

1 Modeling human *TBX5* haploinsufficiency predicts regulatory networks for congenital heart
2 disease

3

4 Irfan S. Kathiriya^{1,2,3*}, Kavitha S. Rao^{1,2,3}, Giovanni Iacono⁴, W. Patrick Devine^{2,5}, Andrew P.
5 Blair^{2,7}, Swetansu K. Hota^{2,3,6}, Michael H. Lai^{2,3}, Bayardo I. Garay^{1,2,3}, Reuben Thomas², Henry
6 Z. Gong⁷, Lauren K. Wasson^{8,9}, Piyush Goyal^{2,3}, Tatyana Sukonnik^{2,3}, Gunes A. Akgun^{2,3}, Laure
7 D. Bernard^{2,3}, Brynn N. Akerberg¹⁰, Fei Gu¹⁰, Kai Li¹⁰, William T. Pu^{10,11}, Joshua M. Stuart⁷,
8 Christine E. Seidman^{8,9}, J. G. Seidman⁸, Holger Heyn^{4,12}, Benoit G. Bruneau^{2,3,6,13*,#}

9

10 1. Department of Anesthesia and Perioperative Care, University of California, San Francisco,
11 CA, USA

12 2. Gladstone Institutes, San Francisco, CA, USA.

13 3. Roddenberry Center for Stem Cell Biology and Medicine at Gladstone, San Francisco, CA,
14 USA

15 4. CNAG-CRG, Centre for Genomic Regulation (CRG), Barcelona Institute of Science and
16 Technology (BIST), Barcelona, Spain;

17 5. Department of Pathology, University of California, San Francisco, CA, USA

18 6. Cardiovascular Research Institute, University of California, San Francisco, CA, USA

19 7. Department of Biomolecular Engineering, University of California, Santa Cruz, Santa Cruz,
20 CA, USA

21 8. Department of Genetics, Harvard Medical School, Boston, MA USA

22 9. Howard Hughes Medical Institute, Division of Cardiovascular Medicine, Brigham and
23 Women's Hospital, Boston, MA USA

24 10. Department of Cardiology, Boston Children's Hospital, Boston, MA, USA

25 11. Harvard Stem Cell Institute, Harvard University, Cambridge, MA, USA

26 12. Universitat Pompeu Fabra, Barcelona, Spain

27 13. Department of Pediatrics, University of California, San Francisco, CA, USA

28 #Lead contact

29 * Correspondence: irfan.kathiriya@ucsf.edu, benoit.bruneau@gladstone.ucsf.edu

30

31 **Abstract**

32 Haploinsufficiency of transcriptional regulators causes human congenital heart disease
33 (CHD). However, underlying CHD gene regulatory network (GRN) imbalances are unknown.
34 Here, we define transcriptional consequences of reduced dosage of the CHD-linked
35 transcription factor, TBX5, in individual cells during cardiomyocyte differentiation from human
36 induced pluripotent stem cells (iPSCs). We discovered highly sensitive dysregulation of TBX5-
37 dependent pathways— including lineage decisions and genes associated with cardiomyocyte
38 function and CHD genetics—in discrete subpopulations of cardiomyocytes. GRN analysis
39 identified vulnerable nodes enriched for CHD genes, indicating that cardiac network stability is
40 sensitive to TBX5 dosage. A GRN-predicted genetic interaction between *Tbx5* and *Mef2c* was
41 validated in mouse, manifesting as ventricular septation defects. These results demonstrate
42 exquisite sensitivity to TBX5 dosage by diverse transcriptional responses in heterogeneous
43 subsets of iPSC-derived cardiomyocytes. This predicts candidate GRNs for human CHDs, with
44 implications for quantitative transcriptional regulation in disease.

45

46 **Keywords**

47 Gene regulation, transcription factor, gene dosage, haploinsufficiency, gene regulatory
48 networks, cardiomyocyte differentiation, congenital heart disease

49

50

51 Introduction

52 CHDs are a leading cause of childhood morbidity and mortality, and incidence of CHDs
53 is estimated to be ten-fold higher in human fetuses of spontaneous termination (Hoffman, 1995;
54 Hoffman and Kaplan, 2002). Many human mutations linked to CHDs are predicted to result in
55 reduced dosage of transcriptional regulators, including transcription factors (TFs) and
56 chromatin-modifying genes (Zaidi and Brueckner, 2017). Despite advances to elucidate the
57 roles of individual factors in heart development and CHDs, how dosage of transcriptional
58 regulators translates to altered GRNs is not known.

59 In humans, homozygous loss of function (LOF) mutations of *TBX5* are not observed in
60 the genome aggregation database of exomes and genomes from large-scale sequencing
61 projects (Karczewski et al., 2020) and is presumed to cause fetal demise. In conjunction, *Tbx5*
62 null mice die of embryonic lethality from severely deformed hearts (Bruneau et al., 2001).
63 Heterozygous mutations in the T-box TF gene *TBX5* cause Holt-Oram syndrome (HOS)
64 (Basson et al., 1997; Li et al., 1997), which uniformly presents with upper limb defects and often
65 with CHDs that include ventricular or atrial septal defects, diastolic dysfunction and arrhythmias.
66 Experiments in mice have revealed a stepwise sensitivity to reductions in *Tbx5* dosage
67 (Bruneau et al., 2001; Mori et al., 2006). These findings demonstrate that a reduction in *TBX5*
68 dosage perturbs downstream gene expression. However, the disrupted regulatory networks and
69 mechanisms are not understood.

70 To build upon findings from mouse models, a tractable human model system is required
71 to study human *TBX5* haploinsufficiency. Human heart tissue from normal, living individuals is
72 largely inaccessible for molecular analysis. As the estimated prevalence of Holt-Oram syndrome
73 is 1:100,000, pathological or surgical specimens from affected patients are very limited.
74 Alternatively, genome editing in human induced pluripotent stem (iPS) cells enables targeted
75 genetic manipulations in an isogenic background. Furthermore, these targeted mutant iPSCs
76 can be differentiated into varied cardiac cell types, including cardiomyocytes, and then

77 subjected to single cell RNA sequencing (RNA-seq). This *in vitro* system provides a promising
78 human cellular platform for gene-centered cardiac disease modeling at single cell resolution.
79 Although iPSC-derived cardiomyocyte differentiation lacks a three-dimensional context for
80 patterning and organization of myriad cell types of the heart, it recapitulates key developmental
81 steps, including mesendoderm and cardiac precursors. Directed cardiomyocyte differentiation
82 leads to a predominance of ventricular cardiomyocytes, with production of some atrial
83 cardiomyocytes and surrounding cell types, such as fibroblasts, endothelial cells and
84 endodermal cells, providing a useful multicellular system to model aspects of human
85 cardiogenesis.

86 In considering how *TBX5* haploinsufficiency might cause CHDs, at least two scenarios
87 are possible: 1. Reduced dosage may only affect genes in vulnerable cell types in specific
88 anatomical locations, such as the ventricular chamber or septum. 2. Reduced dosage may
89 affect cardiac gene expression broadly, but altered programs manifest as morphologic defects
90 only in cell types of anatomic structures most sensitive to the disturbance. The first scenario
91 would be challenging to investigate in two-dimensional cultures, particularly if susceptible
92 region-specific cell types are absent. The second predicts that changes in gene expression
93 might be detected by bulk RNA-seq studies of heterozygous human iPS cell models of CHDs (
94 Theodoris et al., 2015; Ang et al., 2016; Gifford et al., 2019), but relevant, discrete alterations in
95 a complex cell mixture could be missed. Discerning between these scenarios will require a
96 single cell analysis approach.

97 Here, we used an allelic series of *TBX5* in engineered human iPS cells, comprising
98 wildtype, and heterozygous or homozygous loss of function mutations, to investigate GRNs that
99 are altered in response to reduced *TBX5* dosage. We observed *TBX5* dose-dependent cellular
100 phenotypes reminiscent of anomalies in patients with *TBX5* mutations. We deployed single cell
101 RNA-seq across a time course of differentiation and observed that the acquisition of ventricular
102 cardiomyocyte fate is sensitive to *TBX5* dosage. We also discovered discrete gene expression

103 responses to reduced *TBX5* dosage in cardiomyocyte subpopulations. From these data, we
104 identified putative cardiac GRNs that help explain several cellular phenotypes related to human
105 CHD. We validated one of these GRN-predicted genetic interactions in mice. *Tbx5* and *Mef2c*
106 interact to cause muscular ventricular septal defects (VSDs), a common type of human CHD.
107 We conclude that *TBX5* dosage sensitivity, modeled in human iPS cells, reveals discrete gene
108 regulation programs in an unanticipated variety of cardiomyocyte subtypes and informs the
109 biology of human CHD.

110

111 **Results**

112 **Impaired human cardiomyocyte differentiation and function by reduced *TBX5* dosage**

113 To determine a role for *TBX5* dosage in human cardiac biology, we created an isogenic
114 allelic series of human iPS cells mutant for *TBX5*, using CRISPR/Cas9-mediated genome
115 editing to target exon 3 of *TBX5* at the start of the essential T-box domain (Figure S1A, B). We
116 isolated targeted iPS cell lines, including heterozygous (*TBX5*^{in/+}) and homozygous (*TBX5*^{in/del}
117 and *TBX5*^{PuR/PuR}) mutants (Figure 1A, S1C-F). We also isolated a control (*TBX5*^{+/+}) iPS cell line,
118 which was exposed to CRISPR/Cas9 nuclease but not mutated at exon 3 of *TBX5*, to control for
119 off-target effects and the sub-cloning procedure. Subsequently, we refer to wildtype and control
120 collectively as “WT” when significant differences between them were not observed. *TBX5*
121 protein levels in cardiomyocytes differentiated from these lines were diminished in *TBX5*^{in/+} cells
122 and absent in *TBX5*^{in/del} and *TBX5*^{PuR/PuR} cells (Figure 1B), consistent with a dosage-step allelic
123 series of mutant *TBX5* loss-of-function cell lines.

124 We observed reduced cardiomyocyte differentiation efficiency and a delay in onset of
125 beating by loss of *TBX5*, when compared to WT (Figure 1C, D). Worsening sarcomere disarray
126 was seen by stepwise depletion of *TBX5* (Figure 1E-I). Patch clamp analysis of cardiomyocytes,
127 which were predominantly ventricular in this differentiation method, revealed lengthened action
128 potential duration (APD) in *TBX5*^{in/del} cells (Figure 1J, K; action potential duration at 90%

129 repolarization (APD_{90}), adj p-value<0.04 by Holm-Sidak test) (Holm1979), consistent with
130 previous findings (Churko et al., 2018; Karakikes et al., 2017). Although $TBX5^{PuR/PuR}$ cells
131 showed high variability of APD_{90} and were not statistically significantly different from WT, some
132 recordings were distinctly abnormal, displaying striking APD_{90} durations eight times greater than
133 an average wildtype or control cell (Figure 1J, K). Calcium imaging of spontaneously beating
134 cardiomyocytes revealed protracted calcium transient durations in $TBX5^{in/del}$ and $TBX5^{PuR/PuR}$
135 cells (time of 90% decay; (t_{90} down), adj p-value<9E-4 by Holm-Sidak test), with an intermediate
136 defect in $TBX5^{in/+}$ cells (adj p-value<0.01) (Figure 1L, M), implying a potential impairment of
137 cardiomyocyte relaxation. Together, these cellular findings recapitulated several pathological
138 characteristics, which may contribute to diastolic dysfunction in HOS in mice and humans (Zhou
139 et al., 2005; Zhu et al., 2008).

140

141 **Resolving susceptible cardiac cell types from reduced TBX5 dosage**

142 To determine how TBX5 dosage alters gene expression in a heterogeneous cell
143 population, we used a droplet-based single cell RNA-seq method with cells collected from
144 parental WTC11, control $TBX5^{+/+}$, and mutant $TBX5$ ($TBX5^{in/+}$, $TBX5^{in/del}$) genotypes. From three
145 time points during cardiomyocyte differentiation, we interrogated 55,782 cells with an average
146 normalized read depth of 88,234 reads per cell (Figure 2A-C). At day 6, we identified 11 cell
147 clusters, representing at least four cell types, including $POU5F1^+$ pluripotent cells, $MESP1^+$
148 mesoderm, $ISL1^+$ cardiac precursors and nascent $TNNT2^+$ cardiomyocytes (Figure 2D). At day
149 11 and day 23, differentiated cell types were assigned and present in all genotypes (Figure 2E-
150 H, S2A, B), based on cell type-specific marker genes (DeLaughter et al., 2016; Li et al., 2016).
151 This included a diversity of $TBX5^+$ cell types, comprising very few $PLVAP^+$ endothelial cells or
152 TTR^+ endodermal cells, some $COL1A1^+$ fibroblasts and, most abundantly, $TNNT2^+//IRX4^+$
153 ventricular cardiomyocytes (Figure 2E-G, S2A, B).

154 We employed a machine learning algorithm (Pedregosa et al., 2011), to quantitatively
155 evaluate the degree of similarity, if any, between iPSC-derived cells and cells from the
156 developing human heart. A cell type classifier was trained on single cell gene expression from a
157 human fetal four-chambered heart at 6.5-7 weeks gestation (Figure S2C) (Asp et al., 2019).
158 This was used to predict cell type assignments for cells harvested at day 23 (Figure 2I, S2D,
159 Table S1). Ventricular-like cardiomyocytes were the most commonly predicted cell type,
160 constituting 52% of cells from all genotypes, with a high prediction probability average of 0.93,
161 consistent with manual assignments by cell type-specific markers genes, such as *TNNT2* and
162 *IRX4* (Figure 2G, I, S2B, D, E). Twenty-three percent of cells were assigned as fibroblast-like
163 cells with 0.89 probability, 6% as epicardial-like cells with 0.89 probability, and 7% as cardiac
164 cells of neural crest origin with 0.72 probability (Figure 2I, S2D, E). *AFP*⁺ or *TTR*⁺ cells,
165 considered to be derived from endoderm or mesendoderm, were dispersed across several
166 predicted cell assignments (Figure 2I, S2D). As expected, differentiation did not yield iPSC-
167 derived cell types, including erythrocytes (1%) and immune cells (0.2%), which were sparsely
168 represented with less than 0.5 prediction probability (Figure 2I, S2D). Taken together, the
169 classifier's predictions appeared to provide sufficient fidelity for assignments of iPSC-derived
170 cells as *in vivo*-like cardiac cell types.

171 Although the cell type classifier was largely consistent with cell type assignments from
172 manual annotations (Figure 2G, I, S2D), it predicted 9% of iPSC-derived cells from all
173 genotypes as atrial-like cardiomyocytes with a 0.83 probability. Whereas the cell type classifier
174 predicted a similar total number of high-probability (>0.7) cardiomyocytes for each *TBX5*
175 genotype (Figure S2E), more atrial-like cardiomyocytes were predicted for *TBX5*^{in/+} and
176 *TBX5*^{in/del} cells ($p < 0.0001$ by Fisher's exact test), than for WT (Figure S2E). The classifier also
177 uncovered a population of iPSC-derived cardiomyocytes with 'mixed' identity, of both ventricular
178 and atrial predictions. Interestingly, these 'mixed' cardiomyocyte predictions were more
179 prevalent among *TBX5*^{in/+} ($p < 0.001$ by Fisher's exact test) and *TBX5*^{in/del} cells ($p < 0.0001$), than

180 wildtype or control (Figure 2J), supporting a notion that reduced *TBX5* dosage may perturb
181 ventricular cardiomyocyte identity.

182

183 **TBX5 protects human ventricular cardiomyocyte fate**

184 To assess if reduced *TBX5* dosage disturbs paths of directed differentiation, we
185 evaluated supervised URD trajectories from all *TBX5* genotypes and time points. URD predicts
186 cellular chronology based on user-determined origins and ends (Farrell et al., 2018a). We
187 defined *POU5F1*⁺ cells, which were predominantly from a single cluster at day 6 (Figure 2D), as
188 the root and day 23 clusters as the tips in the pseudotime tree (Figure 3A, B). Cells at day 6
189 were found near the top of the tree, while cells at day 11 were distributed mid-way, followed by
190 day 23 cells at the user-defined tips (Figure S3A-C). This demonstrated a logical ordering of
191 cells along pseudotime by URD. Since *TBX5* transcripts were detected in all genotypes,
192 including *TBX5*^{in/del} cells, inferred lineage decisions for *TBX5*⁺ cell types in the absence of *TBX5*
193 could be examined. We focused on inferred trajectories of *TBX5*⁺ cells to ventricular
194 cardiomyocytes. *TBX5*^{in/+} cells followed a path similar to WT (Figure 3C, D, dashed lines), but to
195 a transcriptionally distinct endpoint. In contrast, *TBX5*^{in/del} cells deviated from the WT
196 differentiation path to ventricular cardiomyocytes (Figure 3E).

197 In order to explore gene expression changes that may have led to this deviation, we
198 identified genes that change as a function of pseudotime in the WT or *TBX5*^{in/del} paths (Figure
199 3F). We deduced 22 genes (e.g. electrophysiology-related *NAV1* and *TECRL*, cardiomyopathy-
200 associated *LAMA4*, and small peptide hormone *NPPA*), which were positively correlated with
201 pseudotime in the WT/*TBX5*^{in/+} branch (p-value<0.05 by two-sided *t* test), but aberrant in the
202 *TBX5*^{in/del} branch (Z-score≥15), suggesting that these genes were not activated properly in
203 *TBX5*^{in/del} cells (Figure S3D). Conversely, five genes were negatively correlated in the
204 WT/*TBX5*^{in/+} branch (p-value<0.05 by two-sided *t* test), but not in the *TBX5*^{in/del} branch (Z-
205 score≥15). Likewise, we identified 18 genes that positively (e.g. sarcomere *DES*, vascular

206 adhesion *VCAM1*, and TF *LBH*) or negatively (e.g. TF *HES1* and actomyosin binding *CALD1*)
207 correlated with pseudotime in *TBX5^{in/del}* cells (p-value<0.05), but were altered in wildtype cells
208 (Z-score≥15) (Figure 3G), signifying that these genes were inappropriately deployed in *TBX5^{in/del}*
209 cells.

210 A few ventricular markers (e.g. cardiac TFs *IRX4* and *HEY2*) were absent in *TBX5^{in/del}*
211 cells (Figure 3H, J), reminiscent of features from mouse (Bruneau et al., 2001). However,
212 *TBX5^{in/del}* cells still expressed other ventricular-enriched genes (e.g. cardiac TFs *HAND1* and
213 *HAND2*) (Figure 3H), consistent with their electrophysiologic characteristics as beating
214 ventricular cardiomyocytes (Figure 1J). In conjunction, *TBX5^{in/del}* cells expressed markers of the
215 atrioventricular canal (e.g. cardiac TF *TBX2* and Wnt agonist *RSPO3*) (Figure 3H), indicating
216 that *TBX5* loss results in a disordered ventricular cardiomyocyte-like identity with ectopic gene
217 expression.

218 We tested differential gene expression between intermediate branches, to identify genes that
219 determine *TBX5*-dependent ventricular cardiomyocyte differentiation. We considered these
220 branches as potential precursors proximal to *TBX5* genotype-specific tips. We compared these
221 intermediate branches of cells that distinguish the cell trajectory route of WT and *TBX5^{in/+}* to
222 *TBX5^{in/del}* (Figure 3I). These included secreted factors or cell surface receptors (*WNT2*, *FGFR1*;
223 adj p-value<0.05) and cardiac TFs (*IRX4*, *HAND2*; adj p-value<0.05). Of note, expression of the
224 CHD cardiac transcription factor *NKX2-5*, a transcriptional partner of *TBX5* (Bruneau et al.,
225 2001; Hiroi et al., 2001; Luna-Zurita et al., 2016), was differentially expressed between
226 genotype-enriched intermediate branches of the URD tree (Figure 3J; adj p-value<1E-300 by
227 Wilcoxon Rank Sum test). Consistent with a role of *Nkx2-5* for mouse ventricular cardiomyocyte
228 specification *in vivo* (Lyons et al., 1995; Tanaka et al., 1999), onset of *NKX2-5* expression was
229 delayed in *TBX5^{in/del}* cells (adj p-value<0.05 by Bonferroni-Holm multiple testing correction). In
230 conjunction, a module of genes (chromatin regulator *PARP1*, ribosome *RPL37*, junctional
231 protein encoding *KIAA1462* and Na⁺/K⁺ transport *ATP1A1*; adj p-value<0.05), were expressed

232 concomitantly with *NKX2-5* (Figure S3E, F). This provides a potential molecular explanation for
233 the observed delay in the onset of beating by *TBX5* loss (Figure 1D).

234

235 **Discrete transcriptional responses to reduced *TBX5* dosage in cardiomyocytes**

236 *TBX5* genotype-specific clusters emerged among cardiomyocytes at day 11 (Figure 2B),
237 and *TBX5* genotype-specific segregation was more striking at day 23, particularly in *TNNT2*⁺
238 cells (Figure 2C). Therefore, we focused on *TNNT2*⁺ clusters at day 23 (Figure 4A, B). First, we
239 used a low resolution for Louvain clustering to assess genes that are highly differential between
240 *TBX5* genotype-driven *TNNT2*⁺ clusters (Figure 4C). We detected 121 genes that were
241 differentially expressed between WT and *TBX5*^{in/+}-enriched clusters (Figure 4D, Table S2). Five
242 hundred twenty genes showed differential expression between WT and *TBX5*^{in/del}-enriched
243 clusters (Figure 4E, Table S2). To identify stepwise *TBX5* dose-dependent genes, we evaluated
244 genes that were differentially expressed between WT vs. *TBX5*^{in/+}-enriched clusters and WT vs.
245 *TBX5*^{in/+}-enriched clusters. We found 85 genes common to both lists with a multitude of
246 expression patterns (Figure 4F, Table S2). Many genes displayed changes in both expression
247 level and percentage of expressing cells (e.g. small peptide hormone *NPPA*, Wnt agonist
248 *RSPO3*, arrhythmia-linked *TECRL*, sarcomere *DES*) (Figure 4F). A few genes showed similar
249 levels of gene expression, with changes to percentage of expressing cells (e.g. serine hydrolase
250 *MGLL* or CHD TF *ANKRD1* in *TBX5*^{in/+}-enriched clusters). Some genes, such as *NPPA*, were
251 highly sensitive to *TBX5* dosage, with reduced expression in *TBX5*^{in/+} nearly comparable to that
252 in *TBX5*^{in/del}. In contrast, *TECRL* was partly reduced in *TBX5*^{in/+} cells and was further decreased
253 in *TBX5*^{in/del}. Notably, some genes were altered in *TBX5*^{in/+} cells but had elevated levels in
254 *TBX5*^{in/del} cells (e.g. *TBX5*, myosin light chain *MYL9*, cardiac TF *HOPX*, sarcomere *DES*).
255 Specifically, *TBX5* expression likely reflected apparent upregulation of non-mutated exons in
256 *TBX5*^{in/del} cells, as seen in the mouse (Mori et al., 2006), although *TBX5* protein expression was
257 not detected (Figure 1B). We speculate that expression of other genes with potentially

258 counterintuitive behavior, such as *DES*, may reflect a type of regulatory network compensation
259 or overcompensation, or perhaps indicate a disordered cell type.

260 We used orthogonal assays at single cell resolution to validate examples of TBX5-
261 dependent genes. *TBX5* dosage-dependent downregulation of *NPPA* was evident in
262 cardiomyocytes by RNAscope (*TBX5*^{in/+}, p<0.05; *TBX5*^{in/del} or *TBX5*^{PuR/PuR}, p<1E-4 by Student's
263 t-test) (Figure 4G, H), consistent with the TBX5-dependent rheostatic regulation of *Nppa* in
264 mouse (Bruneau et al., 2001; Mori et al., 2006). By flow cytometry, DES protein was reduced in
265 *TBX5*^{in/+} (p-value<1E-4 by Chi-Square test) and upregulated in *TBX5*^{in/del} (p-value<1E-4 by Chi-
266 Square test) cardiomyocytes, compared to wildtype (Figure 4I-K), corroborating this pattern of
267 *TBX5* dose-dependent expression.

268 To assess the heterogeneity among cardiomyocytes, we used a higher resolution for
269 Louvain clustering and constructed a phylogenetic cluster tree relating 16 different *TNNT2*⁺ cell
270 clusters (Figure 4L, M). We considered these clusters as putative functional subpopulations of
271 ventricular cardiomyocytes, since they could not be classified based on a conventional
272 anatomy-based categorization. We found two clusters (clusters 6 and 10) that included a similar
273 proportion of cells from each *TBX5* genotype, implying that these putative cardiomyocyte
274 subpopulations may be insensitive to reduced TBX5 dosage (Figure 4M, N). We then searched
275 for differentially expressed genes by pairwise comparisons of related subpopulations between
276 *TBX5* genotypes (Figure 4O-U). For example, cluster 5 contains WT and *TBX5*^{in/+} cells (Figure
277 4Q), suggesting that these *TBX5* heterozygous cells are indistinguishable from a subpopulation
278 of WT. In contrast, cluster 7 is largely composed of *TBX5*^{in/+}, suggesting that these TBX5
279 heterozygous cells are distinct. In addition to stepwise TBX5 dose-dependent genes (Figure 4F)
280 that were often altered in many cluster-to-cluster comparisons, we detected additional common
281 changes in gene expression amongst pairwise cluster comparisons of WT vs. *TBX5*^{in/+} clusters.
282 These included the cardiac TF *FHL2*, the cardiomyopathy-linked sarcomere gene *TTN*, and the
283 ventricular-enriched sarcomere gene *MYL2* (Figure 4Q-V; adj p-value<0.05 by Wilcoxon Rank

284 Sum test). We also discerned many differences in gene expression based on cluster-specific
285 comparisons (adj p-value<0.05 by Wilcoxon Rank Sum test), implying varied transcriptional
286 responses among subpopulations of cardiomyocytes to *TBX5* haploinsufficiency (Figure 4Q-V)
287 or *TBX5* loss (Figure 4O, P).

288 These differentially expressed gene sets at day 23 were enriched for electrophysiology
289 (EP) genes (FDR<0.05, Figure 4, Table S2-4), which are implicated in membrane depolarization
290 (*SCN5A*), calcium handling (*RYR2*, *ATP2A2*, and *PLN*) and arrhythmias (*TECRL*) (Figure 4).
291 These genes provide a molecular explanation for the EP defects observed upon *TBX5* mutation.
292 Several altered transcripts were encoded by candidate genes implicated in CHD (e.g. TFs
293 *CITED2*, *MYOCD*, and *ANKRD1*) (Figure 4, Table S2-4) (Homsy et al., 2015; Jin et al., 2017;
294 Lalani and Belmont, 2014; McCulley and Black, 2012; Prendiville et al., 2014; Priest et al., 2016;
295 Sifrim et al., 2016; Zaidi et al., 2013). In addition, some *TBX5*-dependent genes that were
296 previously associated with CHD or arrhythmias by genome-wide association studies (GWAS)
297 were identified (Cordell et al., 2013a; 2013b; Ellinor et al., 2012; Hoed et al., 2013; Hu et al.,
298 2013; Pfeufer et al., 2010a; Smith et al., 2011). We uncovered *IGFBP7*, *MYH7B* and *SMCHD1*
299 for CHD and 45 reported genes for arrhythmias (for example, *PLN*, *HCN4*, *SCN5A*, *GJA1*,
300 *PITX2* and *TECRL*; FDR<0.05) among *TBX5*-sensitive genes (Table S2-4).

301 We assessed if *TBX5* dose-sensitive genes were largely direct or indirect targets of
302 *TBX5*, by examining *TBX5* occupancy in human iPSC-derived CMs from a published dataset
303 (Ang et al., 2016). We found correlations of *TBX5* occupancy near *TBX5* dosage-vulnerable
304 gene sets at day 23 (Figure 4, bolded genes; Figure S4A-F, Table S4). For example, 61 of 85
305 genes that showed stepwise dose-dependence were near *TBX5* binding sites (Figure 4F, Figure
306 S4A), suggesting that these genes were predicted targets of *TBX5*. *TBX5* cooperates with
307 *GATA4* for cardiac gene regulation (Ang et al., 2016; Garg et al., 2003; Luna-Zurita et al., 2016).
308 We also observed a high association of *GATA4* occupancy with *TBX5* (Ang et al., 2016) near

309 TBX5-dependent genes (Figure S4A-E, Table S4, 5), indicating that GATA4 may have a role in
310 modulating TBX5 dosage-sensitive genes.

311 Since modifiers in different genetic backgrounds can modulate phenotypic effects, we
312 assessed alternatively targeted iPSC lines of *TBX5* mutants in an independent genetic
313 background (PGP1, from a Caucasian male (Lee et al., 2009), compared to WTC11 from a
314 Japanese male (Miyaoaka et al., 2014), Figure S5A, B). We independently evaluated
315 comparisons between genotype-enriched subtype clusters in day 23 *TNNT2*⁺ cells from PGP1-
316 derived cell lines (Figure S5C-G). Comparisons of lists of TBX5-dependent genes in day 23
317 *TNNT2*⁺ cells showed overlap between WTC11 vs. *TBX5*^{in/+} and PGP1 vs. *TBX5*^{in/+} ($p < 5.219e$ -
318 81 by hypergeometric test), or WTC11 vs. *TBX5*^{in/del} and PGP1 vs. *TBX5*^{del/del} ($p < 1.438e$ -172).

319 We also integrated day 23 *TNNT2*⁺ cells from each genetic background into one
320 combined dataset for analysis. Cells were largely indistinguishable in UMAP space regardless
321 of experimental replicate or genetic background (Figure S5H). Importantly, we again observed
322 segregation by *TBX5* genotypes (Figure S5I). By comparing genotype-enriched subtype clusters
323 (Figure S5J, K), we detected 148 genes between WTC11/Control/PGP1 and *TBX5*
324 heterozygous cells, and 457 genes between WTC11/Control/PGP1 and *TBX5* homozygous
325 cells (Figure S5L, M, Table S2). These results demonstrated robust TBX5 dosage-dependent
326 gene expression alterations in cardiomyocytes from independent experiments, genetic
327 backgrounds, and gene targeting strategies. Any differences in gene expression between
328 biological replicates and genetic backgrounds likely reflected a combination of technical
329 variability, biological stochasticity or genetic modifiers that, as in patients with *TBX5* mutations
330 (Basson et al., 1994), may explain variable expressivity of disease for a given mutation.

331

332 **TBX5 dosage maintains cardiac gene network stability**

333 CHD-associated and arrhythmia-related genes were enriched among TBX5-dependent
334 genes in complex patterns of expression. We sought to independently, and without bias, assess

335 the importance of *TBX5* in a global cardiac gene regulatory network (GRN) beyond changes to
336 gene expression. To evaluate the role of *TBX5* dosage for regulating GRNs, we used bigSCale2
337 (Iacono et al., 2019) to independently infer putative GRNs without *a priori* knowledge (e.g.
338 protein-protein interactions, known genetic associations, cardiac-enriched genes) from single
339 cell expression data of *TNNT2*⁺ cells. By applying the concept of “pagerank”, first devised to
340 rank the importance by popularity of websites via numerical weighting (Brin and Page, 1998),
341 we predicted quantitatively the biological importance (i.e. centrality) of genes in a GRN, even if a
342 node’s gene expression was unchanged by *TBX5* dosage.

343 By comparing inferred networks of WTC11 and Control to *TBX5*^{in/+} or *TBX5*^{in/del} within a
344 given time point, we uncovered several candidate nodes that displayed loss of pagerank
345 centrality from reduced *TBX5* dosage (Figure 5A-C, S6A-D Table S6). These included the
346 calcium-handling gene *RYR2*, and twenty CHD genes (for example, TFs *GATA6*, *HAND2*, and
347 *SMAD2*, $p < 2.2e-5$ by hypergeometric test,) (Figure 5C), consistent with our analysis from
348 differential gene expression. For example, at day 11, pagerank centrality of the CHD TF *SMAD2*
349 was absent in *TBX5*^{in/+} cells (Figure 5A-C, top 5% of all changes), indicating a possible
350 impairment of *SMAD2* function from *TBX5* haploinsufficiency. Centrality of the cardiac
351 development-related TF *MEF2C*, which is necessary for mouse heart development (Lin et al.,
352 1997), was substantially reduced by heterozygosity or loss of *TBX5* at day 11 (Figure 5A-C, top
353 5% cutoff). Quantitative alterations to GRNs showed that *TBX5* dosage may be critical for
354 maintaining cardiac network stability, and potentially unveiled putative genetic interactions
355 disrupted in *TBX5*-dependent CHDs.

356 To further investigate the predicted relationship between *TBX5* and *MEF2C* within a
357 human *TBX5* dosage-sensitive, CHD-associated GRN, we used a complementary approach
358 using bigSCale2, to identify gene-gene correlations with *TBX5* expression in individual *TNNT2*⁺
359 cells across timepoints and *TBX5* genotypes (Figure 5D). Genes highly co-expressed with *TBX5*
360 (Pearson coefficient >0.5) regardless of *TBX5* genotype suggested potential positive regulation

361 or possible cell autonomous effects by *TBX5* dosage (for example, calcium-handling *PLN* and
362 *RYR2*, and sarcomere *TTN*), while those with high anti-correlation (Pearson coefficient <-0.5)
363 suggested potential negative regulation or possibly non-cell autonomous effects (for example,
364 TFs *HES1*, *TLE1*, *CBX1*, *ETV4*, *ID4*, and cell surface receptor *FGFR1*). *MEF2C* expression was
365 among the highest correlated with *TBX5* expression and demonstrated the greatest *TBX5*-
366 dependent decrease of pagerank at day 11 (Figure 5D, Table S6), further suggesting *MEF2C* as
367 a putative candidate for mediating *TBX5* dose-sensitive regulatory effects.

368 *MEF2C* gene expression itself was unchanged by reduced *TBX5* dosage. Yet, *MEF2C*
369 also displayed the greatest *TBX5*-dependent decrease in degree centrality, which reflects a
370 node's connections in a network and contributes to pagerank, at day 11 (Figure 5E, Table S6).
371 This indicated potential alterations to *MEF2C* functional connectivity within the *TBX5*-dependent
372 GRN. We found that multiple genes, which correlated with *MEF2C*, displayed diminished levels
373 of degree by reduced *TBX5* dosage (e.g. transcriptional regulators *SMYD1* and *MYOCD*,
374 sarcomere *TTN*, calcium-handling *RYR2*, and kinase *PDK1*; top 5% cutoff) (Figure 5F, Table
375 S6). Some genes (*SMYD1* and *MYOCD*) are direct *MEF2C* targets in mice *in vivo* (Creemers et
376 al., 2006; Phan et al., 2005). This suggested to us that these candidate genes with reduced
377 degree may mediate putative *MEF2C* functional connectivity for *TBX5* dosage-sensitive GRNs.

378

379 ***Tbx5* and *Mef2c* cooperate for ventricular septation *in vivo***

380 Several potential genetic interactions were predicted by reduced pagerank from *TBX5*
381 dose-dependent human GRNs. A predicted genetic interaction between *Tbx5* and *Gata6* is
382 known from mouse studies (Maitra et al., 2009). However, heterozygous loss of *Tbx5* can lead
383 to highly penetrant perinatal lethality based on mouse genetic background strains (Bruneau et
384 al., 2001; Mori et al., 2006), making it difficult to evaluate genetic interactions based on
385 postnatal lethality. Therefore, we further characterized a multifunctional allele of *Tbx5*
386 (*Tbx5*^{CreERT2IRES2xFLAG}, abbreviated *Tbx5*^{CreERT2}) (Devine et al., 2014a), which appeared to be a

387 hypomorphic *Tbx5* allele, as a potential genetic tool for probing highly-sensitive *in vivo* genetic
388 interactions with *Tbx5* (Figure 6). Mice heterozygous for *Tbx5*^{CreERT2IRES2xFLAG} (*Tbx5*^{CreERT2/+})
389 survived to adulthood, and Mendelian ratios were recovered at weaning, as well as during
390 embryonic development (Figure 6A). However, embryos homozygous for *Tbx5*^{CreERT2IRES2xFLAG}
391 (*Tbx5*^{CreERT2/CreERT2}) could only be recovered until embryonic day 16.5 (E16.5), indicating that the
392 *Tbx5*^{CreERT2IRES2xFLAG} allele is likely hypomorphic (Figure 6B). Histological analysis of embryonic
393 *Tbx5*^{CreERT2/CreERT2} hearts at E16.5 showed atrioventricular canal (AVC) defects, which include
394 atrial septal defects (ASDs), VSDs and an atrioventricular valve (AVV), which were not present
395 in wildtype or *Tbx5*^{CreERT2/+} mice, implicating CHDs as the cause of late embryonic lethality
396 (Figure 6C -F).

397 *MEF2C* was a quantitatively important node in human TBX5-dependent GRNs.
398 Accordingly, we evaluated a predicted genetic interaction between *TBX5* and *MEF2C* in an *in*
399 *vivo* mammalian context. Using the hypomorphic allele of *Tbx5* and a null allele of *Mef2c*
400 (*Mef2c*^{del}) (Lin et al., 1997), we noted that *Tbx5*^{CreERT2/+};*Mef2c*^{del/+} mice were underrepresented at
401 weaning (Figure 6G). By histology, we detected a highly penetrant morphologic phenotype of
402 ventricular septal defects (n=4 of 4), consisting of muscular (n=3 of 4) or membranous (n=1 of
403 4) VSDs, in compound heterozygous embryos at E14.5. VSDs were not observed in
404 *Tbx5*^{CreERT2/+} or *Mef2c*^{del/+} littermate embryos (Figure 6H-Q). Muscular VSDs are rarely observed
405 in mouse models of CHD, making this observation particularly compelling. These findings
406 demonstrate a highly-sensitive genetic interaction between *Tbx5* and *Mef2c* in mouse *in vivo*,
407 consistent with predictions from a human TBX5 dose-sensitive GRN.

408 We speculated that MEF2C may play a direct role to co-regulate TBX5-dependent gene
409 expression during heart development. Using mice targeted with a FLAG-biotin (fl-bio) tag at
410 specific TF loci, chromatin occupancy (Akerberg et al., 2019) of TBX5, MEF2C, and MEF2A
411 (also predicted to be part of the TBX5-dependent GRN, Table S6) was highly correlated near
412 mouse orthologs of TBX5-sensitive human genes (for example, *HAND2*, *FHL2*, *TECRL*,

413 *NPPA/NPPB*; Figure 6R-U; Tables S7-8, FDR<0.05 for multiple comparisons). Thus, direct co-
414 regulation of target genes by *TBX5*, *MEF2C*, and *MEF2A*, in addition to previously known co-
415 occupancy with *NKX2-5* and *GATA4* (Ang et al., 2016; Luna-Zurita et al., 2016), may be a
416 potential *TBX5* dosage-dependent mechanism for *TBX5* haploinsufficiency.

417

418 **Discussion**

419 Our studies with a human cellular model of *TBX5* haploinsufficiency has defined
420 consequences of reduced *TBX5* dosage during cardiomyocyte differentiation at single cell
421 resolution, indicating a dose-sensitive requirement of *TBX5* for human ventricular cardiomyocyte
422 differentiation and function. Of potential relevance to a range of anatomical and functional
423 manifestations of *TBX5* haploinsufficiency, we uncovered discrete responses to reduced *TBX5*
424 dosage in susceptible ventricular cardiomyocyte subsets. The quantitative specificity of *TBX5*-
425 dependent cell types underscores cellular complexity in response to reduced transcription factor
426 dosage. Many of the cellular phenotypes of this human disease model are cardiomyocyte-
427 specific, intrinsic and likely cell autonomous. Dysregulated gene expression of EP or CHD
428 genes provide potential molecular explanations for these cellular phenotypes, which are
429 relevant to HOS, and more broadly to CHDs, in humans.

430 We found that *TBX5* dosage was necessary for preserving ventricular cardiomyocyte
431 identity. We leveraged machine learning to predict assignments of iPSC-derived cells from a
432 classification of human fetal heart cell types (Asp et al., 2019), lending support to the notion that
433 our human disease modeling may serve as a reasonable proxy to study human cardiogenesis
434 using molecular genetics. We predicted a mixed ventricular-atrial cardiomyocyte identity *in vitro*,
435 which was exacerbated by *TBX5* loss. In addition, developmental trajectory inferences
436 highlighted how a path to ventricular cardiomyocyte fate was vulnerable to reducing *TBX5*
437 dosage.

438 Susceptibility to *TBX5* dosage-dependent gene expression in specific regions of the
439 developing heart was apparent from studies modeling *TBX5* haploinsufficiency in the mouse
440 (Bruneau et al., 2001; Mori et al., 2006). The implication would be that discrete populations in
441 the developing human heart would respond specifically to reduced *TBX5* dosage. In support of
442 this notion, with single cell resolution of gene expression in human iPSC-derived
443 cardiomyocytes, we detected discrete changes to reduced *TBX5* dosage in apparent
444 subpopulations of human ventricular cardiomyocytes. The richness of detail achieved here
445 eclipses current knowledge of *TBX5* haploinsufficiency from mouse models.

446 Many *TBX5*-sensitive genes that we discovered are related to heart function. CHDs are
447 largely viewed as three-dimensional structural defects, but they are often accompanied by
448 cardiac dysfunction, even after surgical correction. Arrhythmias and diastolic dysfunction are
449 observed in patients with HOS (Basson et al., 1994; McDermott et al., 2008; Mori and Bruneau,
450 2004; Zhu et al., 2008), and in many other types of CHDs not related to *TBX5* (Panesar and
451 Burch, 2017). Furthermore, *TBX5* is strongly associated with EP defects based on genome-wide
452 association studies (Ellinor et al., 2012; Pfeufer et al., 2010b; Smith et al., 2011). *TBX5* dosage
453 has been shown to be necessary for preserving diastolic function in mice, by modulating
454 *SERCA2a*-dependent calcium transients (Zhu et al., 2008), and regulating calcium cycling in
455 atrial myocytes in the context of atrial fibrillation (Dai et al., 2019; Laforest et al., 2019; Nadadur
456 et al., 2016). In our iPSC cell model, cardiomyocytes showed *TBX5* dose-sensitive slowing of
457 decay of calcium transients and disarray of sarcomeres, likely reflecting impaired ventricular
458 cardiomyocyte relaxation. In these cells, dysregulation of several genes responsible for calcium
459 cycling, including the *SERCA2*-encoding gene *ATP2A2*, *NCX1*-encoding gene *SLC8A1*, *RYR2*,
460 and *PLN*, provide a potential molecular explanation for ventricular cardiomyocyte impairment
461 and diastolic dysfunction in HOS (Eisner et al., 2020). Notably, the arrhythmia-associated gene
462 *TECRL* displayed stepwise dosage-dependent sensitivity to reduced *TBX5* and is a predicted
463 *TBX5* target. Loss of *TECRL* in human iPSCs leads to prolonged calcium transients (Devalla et

464 al., 2016), comparable to reducing TBX5 dosage. An understanding of TBX5 function in calcium
465 homeostasis may uncover new mechanisms for human arrhythmogenesis and potentially for
466 ventricular cardiomyocyte relaxation.

467 Many CHD genes were found to be altered due to reduced TBX5 dosage. This implies
468 an interconnected network of CHD genes, potentially modulating each other's functional targets.
469 To gain an unbiased view into potential TBX5-sensitive networks, we inferred TBX5-dependent
470 GRNs from individual human *TNNT2*⁺ cells during a differentiation time course, from nascent to
471 beating cardiomyocytes. We measured quantitative metrics for nodes of centrality, such as
472 pagerank and degree (Iacono et al., 2019), and evaluated changes to each node by *TBX5*
473 genotype and time point. Importantly, these quantitative measures of centrality are not defined
474 by any *a priori* knowledge of cardiac biology, and stem solely from the single cell RNA-seq data.
475 Quantitative analysis of human TBX5 dose-sensitive GRNs predicted vulnerable nodes enriched
476 for CHD or cardiac development genes, suggesting a vital role for TBX5 dosage to maintain
477 cardiac network stability. The sensitivity of a GRN to transcription factor dosage has been
478 observed in *Drosophila* embryo patterning (Stathopoulos and Levine, 2002), for example, but
479 has not been linked to human disease to date.

480 From TBX5-sensitive GRNs, we discovered several important nodes linking many CHD
481 genes. For example, reduced centrality of *MEF2C* in the TBX5-dependent GRN predicted an
482 important and sensitive genetic link between these cardiac transcription factors. Consistent with
483 this notion, double-knockdown of *tbx5* and *mef2c* in zebrafish lead to severe defects in the
484 looping heart tube (Ghosh et al., 2009). We observed a strikingly sensitive genetic interaction of
485 *Tbx5* and *Mef2c* in mice using a hypomorphic allele of *Tbx5* (Devine et al., 2014b) and a null
486 allele of *Mef2c* (Lin et al., 1997). This genetic interaction unveiled a finely tuned role later in
487 mammalian heart development, beyond heart looping and chamber formation, for the process of
488 ventricular septation. Of note, the *Tbx5* and *Mef2c* genetic interaction in mouse yielded
489 muscular VSDs, a very specific type of CHD that is rarely observed in mouse models but

490 common in humans. We anticipate that these and other genetic interactions will allow the
491 discovery of molecular pathways and cellular processes that underlie specific CHDs.

492 While many *TBX5*-dependent genes were consistent across two ethnically diverse
493 genetic backgrounds, there were some apparent differences. This is consistent with a notion
494 that modifiers in genetic backgrounds can contribute to varying degrees of phenotypic
495 expressivity for CHDs. Furthermore, variability in CHDs with monogenic inherited or *de novo*
496 mutations could be explained by additional mutations or copy number variations of genes that
497 form part of these functional regulatory networks, as illuminated by our findings, and as
498 evidenced by oligogenic inheritance of CHD-causing variants (Gifford et al., 2019). Our results
499 point to a genomic framework that will guide genetic insights into the underpinnings of CHD.
500 The biophysical rules relating to transcription factor binding and dosage sensitivity are only now
501 becoming understood. Our results in a human cellular model of *TBX5* haploinsufficiency may
502 potentially bring immediate pertinence of human disease to this biological context.

503

504 **Contributions.** I.S.K. and B.G.B conceived and designed the project. B.I.G., L.W., L.B., T.S.
505 and I.S.K. performed gene targeting and isolation of mutant iPSCs. B.I.G., K.S.R., P.G., T.S.,
506 and I.S.K. performed in vitro differentiation and harvested samples. P.G. performed the
507 Western analysis. M.H.L. performed electrophysiology analyses. R.T. performed statistical
508 analyses for electrophysiology. K.S.R. performed immunostaining and scoring of
509 cardiomyocytes. G.A.A. performed RNAscope and flow cytometry. K.S.R., A.P.B. and I.S.K.
510 performed Seurat analysis. K.S.R., A.P.B., H.Z.G., and I.S.K. performed pseudotime analyses.
511 A.P.B. employed machine learning for the cell type classifier. H.Z.G. implemented the cell
512 browser. G.I. performed gene regulatory network analyses. W.P.D. and I.S.K. performed
513 phenotype analyses of mutant mice. B.N.A., F.G., K.L., and W.T.P. performed ChIP-seq
514 experiments and peak calling. S.K.H. and R.T. performed association analyses of co-
515 occupancy, gene expression and disease candidates. J.M.S., W.T.P., C.E.S., J.G.S., and H.H.

516 provided advising. I.S.K. and B.G.B. wrote the manuscript, with comments and contributions
517 from all authors.

518

519 **Acknowledgements.** We thank Dario Miguel-Perez and Sarah Wood for mouse genotyping
520 and colony maintenance, Jeff Farrell for input on URD, David Joy and Todd McDevitt for sharing
521 in-house imaging software, Brian Black for mouse lines, Kathryn Claiborn for editorial
522 assistance, and members of the Bruneau lab for discussions and comments. We also thank the
523 Gladstone Bioinformatics, Genomics, Histology and Microscopy, and Stem Cell Cores, the
524 UCSF Laboratory for Cell Analysis, the UCSF Center for Advanced Technology, the Salk
525 Institutes Center of Excellence for Stem Cell Genomics, Matthew Speir and Maximilian
526 Haeussler at cells.ucsc.edu, and the UCSC Stem Cell Data Center Hub for their invaluable
527 assistance. This work was supported by grants from the National Institutes of Health (NHLBI
528 Bench to Bassinet Program UM1HL098179 to B.G.B. and UM1HL098166 to J.G.S., C.E.S. and
529 W.T.P.; R01HL114948 to B.G.B., USCF CVRI 2T32HL007731-27 to S.K.H), the California
530 Institute for Regenerative Medicine (RB4-05901 to B.G.B), the Office of the Assistant Secretary
531 of Defense for Health Affairs through the Peer Review Medical Research Program under Award
532 No. W81XWH-17-1-0191 (B.G.B), the Foundation for Anesthesia Education and Research
533 (Mentored Research Training Grant to I.S.K.), Society for Pediatric Anesthesia (Young
534 Investigator Award to I.S.K.), Hellman Family Fund (I.S.K.), UCSF REAC Grant (I.S.K.) and
535 UCSF Department of Anesthesia and Perioperative Care (New Investigator Award to I.S.K.).
536 H.H. is a Miguel Servet (CP14/00229) researcher supported by the Spanish Institute of Health
537 Carlos III (ISCIII) and Ministerio de Ciencia, Innovación y Universidades (SAF2017-89109-P;
538 AEI/FEDER, UE). This work was also supported by an NIH/NCRR grant (C06 RR018928) to the
539 J. David Gladstone Institutes, and the Younger Family Fund (B.G.B.). Opinions, interpretations,
540 conclusions and recommendations are those of the author and are not necessarily endorsed by
541 the Department of Defense. In conducting research using animals, the investigator(s) adheres

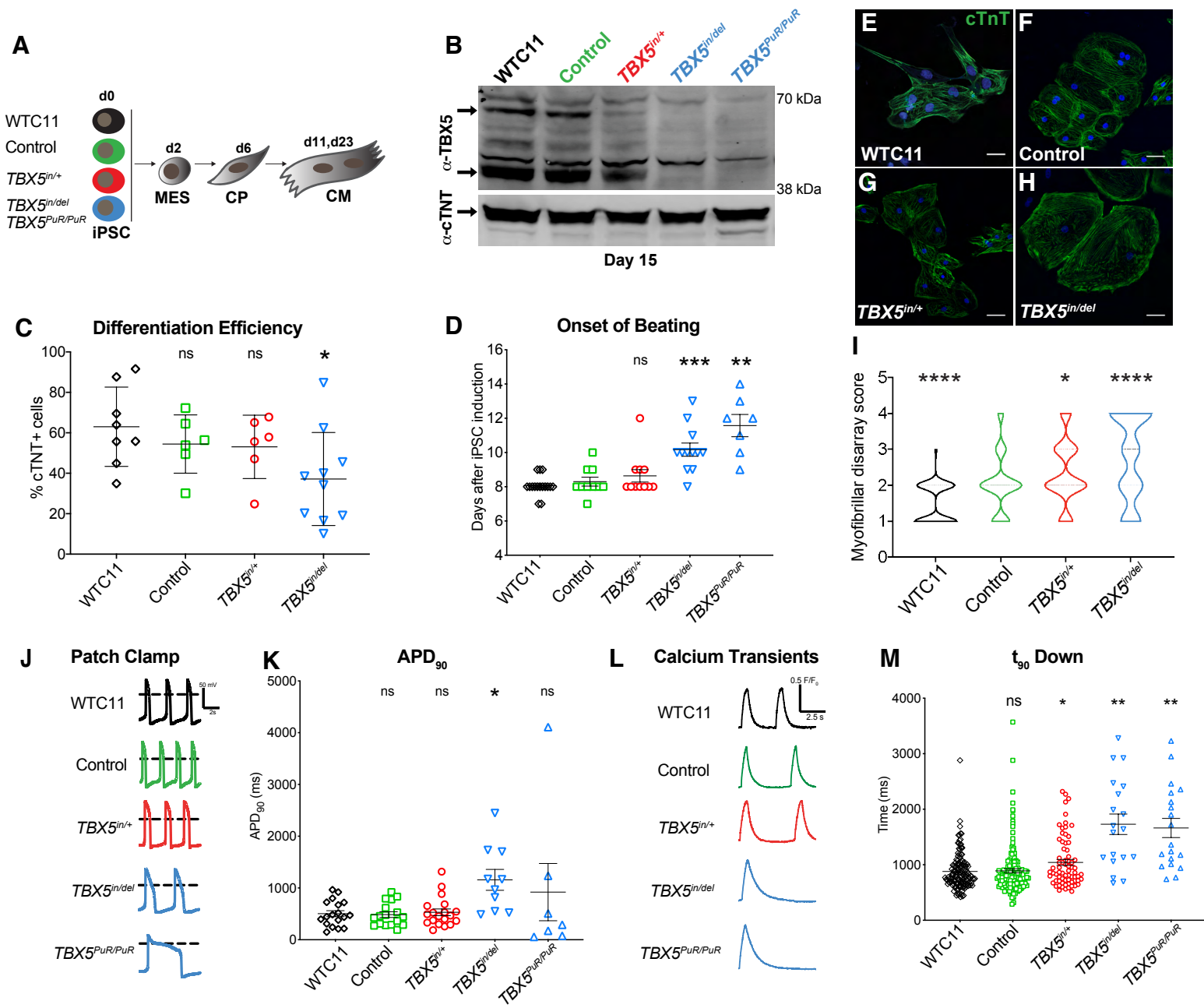
542 to the laws of the United States and regulations of the Department of Agriculture. In the conduct
543 of research utilizing recombinant DNA, the investigator adhered to NIH Guidelines for research
544 involving recombinant DNA molecules.

545

546 **Competing Interests:** B.G.B. is a co-founder and shareholder of Tenaya Therapeutics. None of
547 the work presented here is related to the interests of Tenaya Therapeutics.

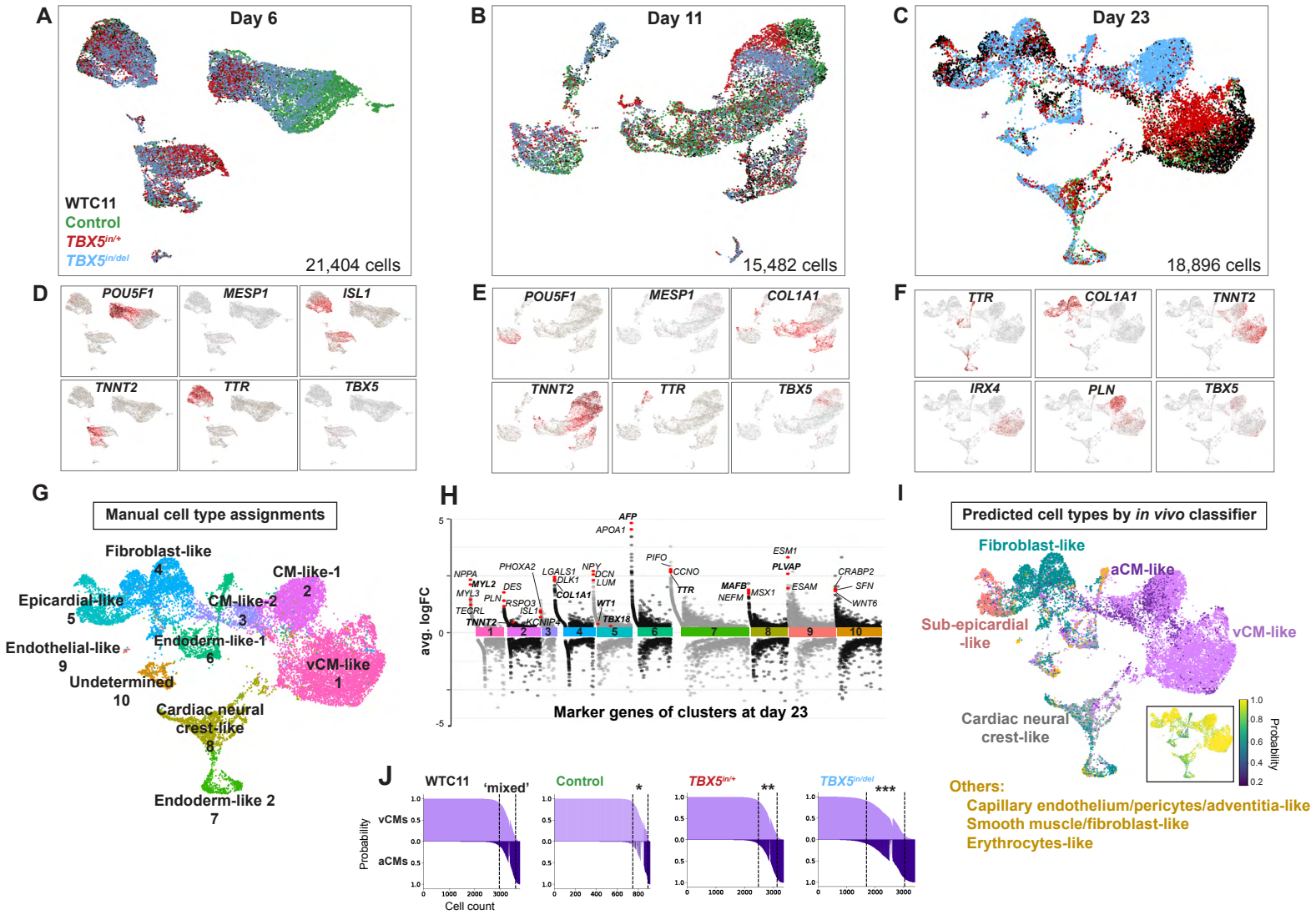
548

Figure 1



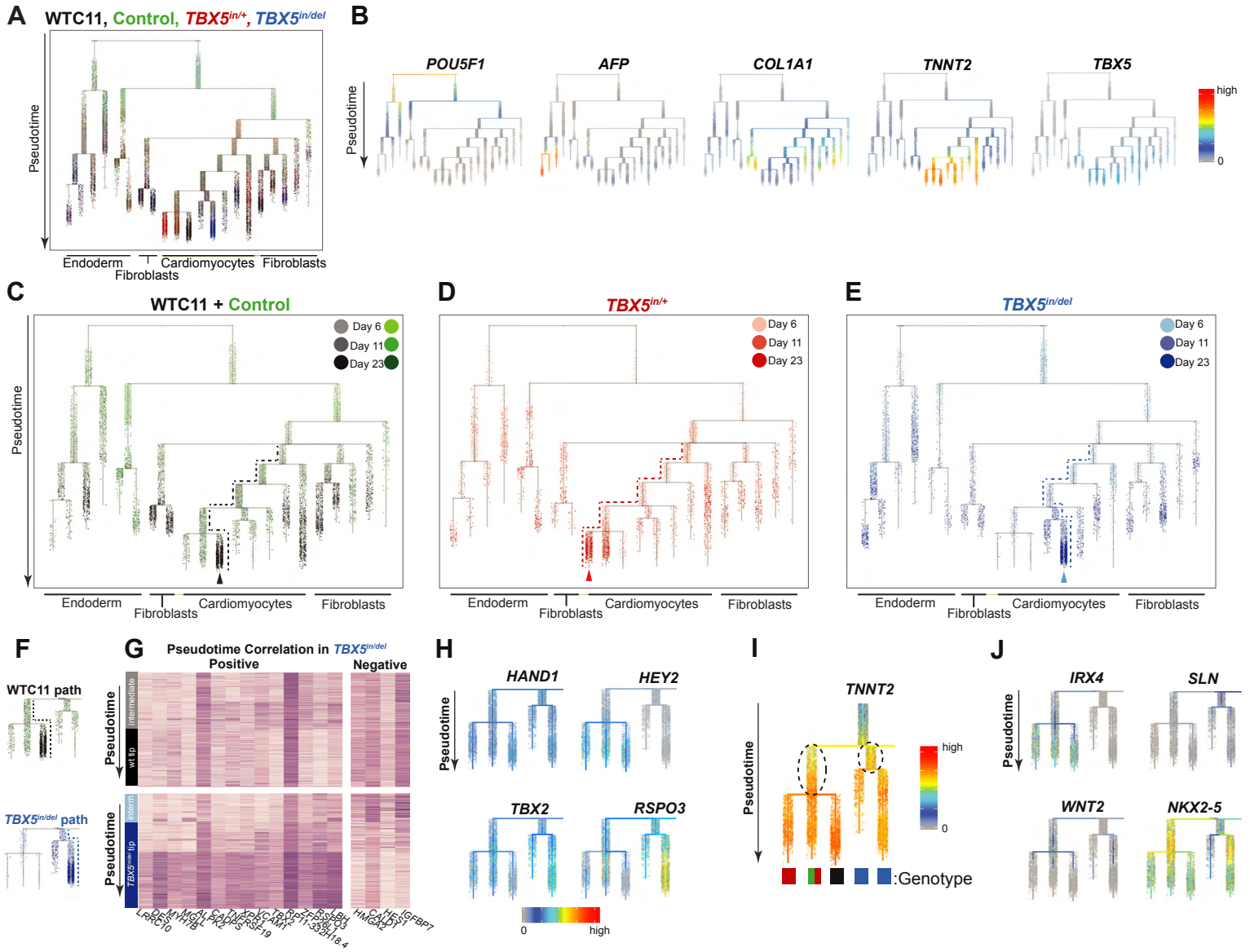
549 **Figure 1. A human allelic series of *TBX5* mutants model features of congenital heart**
550 **disease.** (A) Parental iPS cell line WTC11, control (CRISPR-treated, unmodified at exon 3 of
551 *TBX5*) and targeted *TBX5* loss of function mutants (*TBX5*^{in/+}, *TBX5*^{in/del}, or *TBX5*^{PuR/PuR})
552 underwent directed differentiation to cardiomyocytes (CM) via mesoderm (MES) and cardiac
553 precursor (CP) stages. (B) *TBX5* and cTNT protein expression for each *TBX5* genotype from
554 the cardiomyocyte stage at day 15. (C) Differentiation efficiency by flow cytometry for cTNT⁺
555 cells (* p-value<0.05 by unpaired *t* test). (D) Onset of beating (** p-value<0.01, *** p-
556 value<0.001 by unpaired *t* test). (E-I) Myofibrillar arrangement of cardiomyocytes (* p-
557 value<0.05, **** p-value<0.0001 by Fisher's exact test). (J) Action potentials by patch clamp of
558 single beating cells for each *TBX5* genotype. (K) Action potential duration at 90% (APD₉₀) (*
559 FDR<0.05). (L, M) Traces of calcium transients from single or small clusters of beating cells
560 were analyzed, including time at 90% decay (t₉₀ down) (* FDR<0.05, ** FDR<0.01). Error bars
561 represent standard deviation (J, K) or standard error (L, M) of the mean. Data for *TBX5*^{PuR/PuR} is
562 shown where available.
563

Figure 2



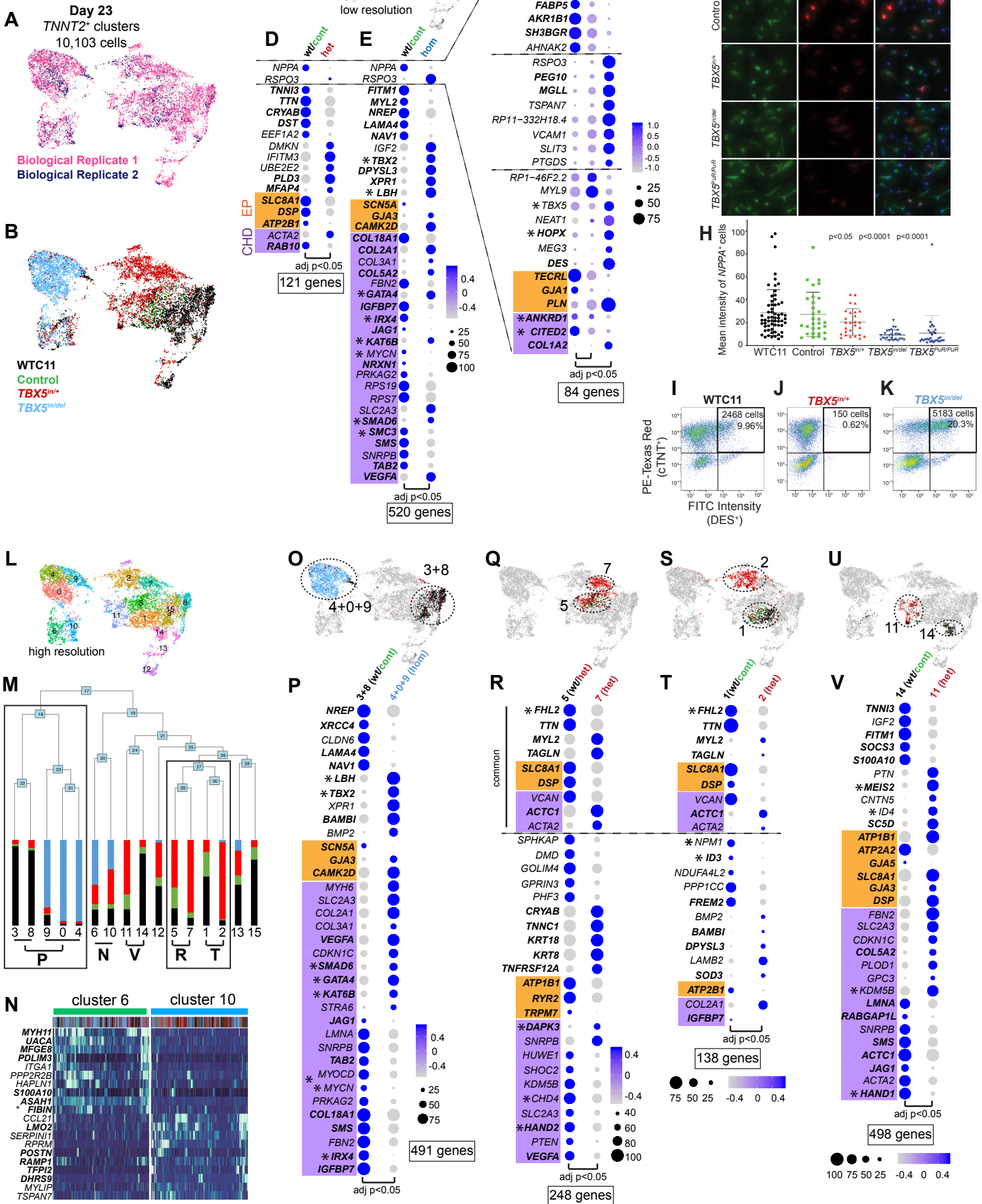
564 **Figure 2. Human cardiomyocyte differentiation is sensitive to reduced TBX5 dosage.** (A-
565 C) Cells of each *TBX5* genotype were harvested at specific stages during directed differentiation
566 to cardiomyocytes for single cell RNA-seq. UMAPs display cells of *TBX5* genotypes at day 6,
567 day 11 or day 23. (D-F) Feature plots in UMAP space demonstrate expression of selected
568 marker genes, which represent major cell types at each timepoint. (G) Cell type assignments of
569 iPSC-derived cells at day 23 by manual annotation using marker genes are shown in UMAP
570 space. (H) A Manhattan plot displays differentially expressed genes by cell type cluster at day
571 23. Examples of enriched genes by cluster are shown. Manual annotation was based on
572 expression of bolded genes. (I) Predicted cell types of iPSC-derived cells at day 23 are
573 classified using machine learning, based on human fetal cardiac cells *in vivo* (Asp et al., 2019).
574 Inset of UMAP shows prediction probabilities for iPSC-derived cells at day 23 by the *in vivo* cell
575 type classifier. (J) Waterfall plots for each *TBX5* genotype display prediction probabilities of
576 iPSC-derived cells classified as ventricular cardiomyocytes (vCM), atrial cardiomyocytes (aCM)
577 or mixed (<0.95 probability difference of vCM and aCM). * p<0.01, ** p<0.001, *** p<0.0001 by
578 Fisher's exact test.
579

Figure 3



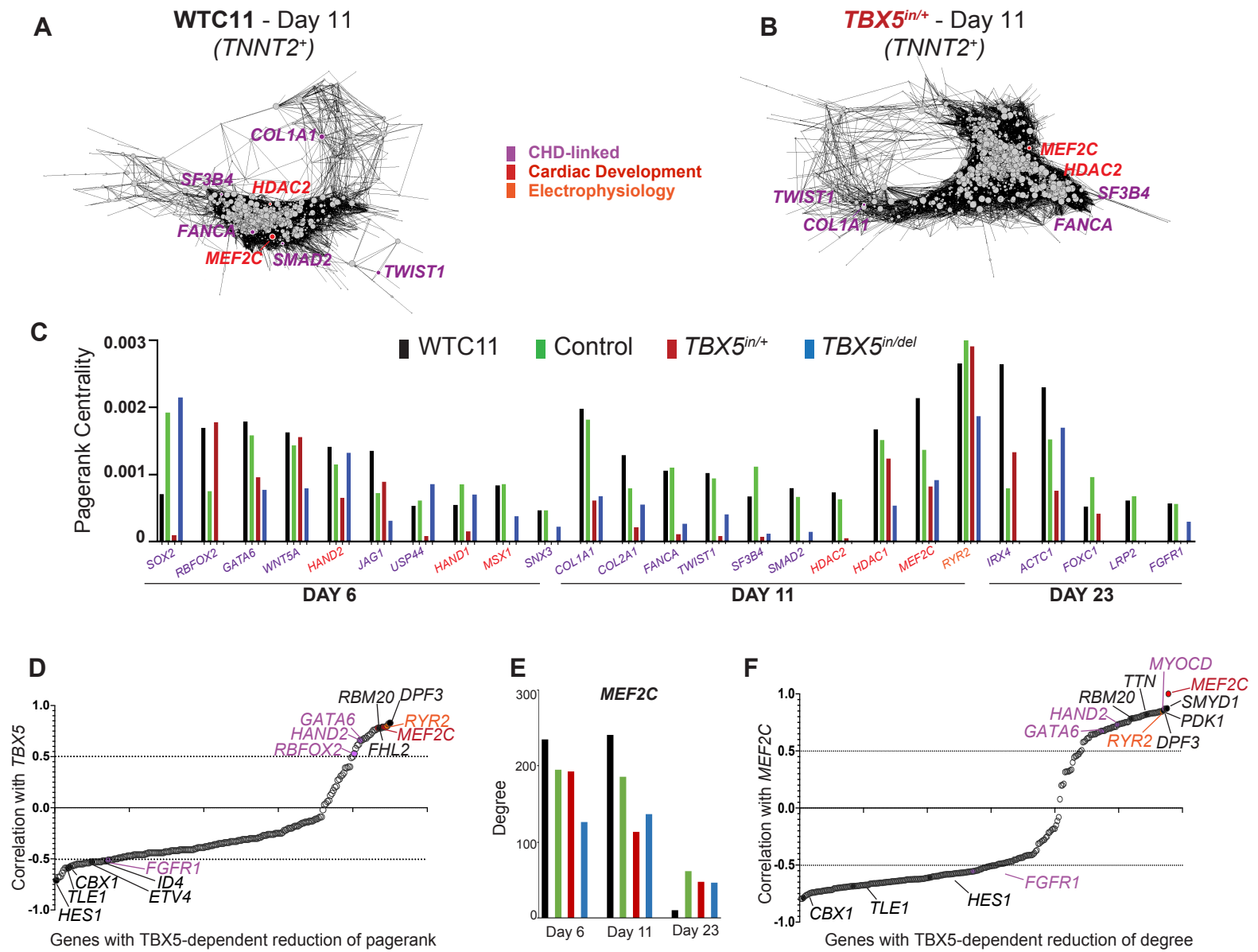
580 **Figure 3. *TBX5* loss disturbs cell trajectories to ventricular cardiomyocyte fate.** (A)
581 Developmental trajectories were inferred by URD using a combined dataset of all *TBX5*
582 genotypes and time points. A dendrogram shows cells at day 6, 11 and 23, during directed
583 differentiation to cardiomyocytes. Pseudotime is displayed from root (top) to tips (bottom). Each
584 *TBX5* genotype is color-coded from light to dark, to indicate the time point. (B) Expression of
585 genes that define the major cell types (pluripotent cell, endoderm, fibroblast and cardiomyocyte)
586 and *TBX5* are shown. (C-E) Cells are highlighted by *TBX5* genotype on the aggregate
587 pseudotime dendrogram. Note the enrichment or depletion of cells from one genotype at certain
588 branch points to tips (arrowheads). Dashed lines show a path to ventricular cardiomyocytes, by
589 *TBX5* genotype. (F) Deduced paths to non-dividing cardiomyocytes of WT (black dashed line) or
590 *TBX5^{in/del}* (blue dashed line) are shown, from intermediates (labeled 'interm') to tips. (G)
591 Heatmaps show expression for each gene that displays no correlation with pseudotime in the
592 WT path (above), but a positive or negative correlation ($|\rho| \geq 0.4$ and Z-score ≥ 15 by difference
593 in ρ) in the *TBX5^{in/del}* path (below). (H) Feature plots show the WT or *TBX5^{in/del}* path for
594 ventricular cardiomyocyte-enriched genes *HAND1* and *HEY2*, and atrioventricular canal-
595 enriched genes *TBX2* and *RSPO3*. (I) Differential gene expression of inferred precursors for the
596 cardiomyocyte branches (dashed ovals) show several genes that display altered gene
597 expression (adj p-value < 0.05 by Wilcoxon Rank Sum test) along the deduced WT or *TBX5^{in/del}*
598 path. Colored blocks below the dendrogram represent the predominant *TBX5* genotypes in each
599 tip. (J) The ventricular cardiomyocyte-enriched gene *IRX4* was absent along the *TBX5^{in/del}* path.
600 *SLN* was qualitatively enriched in the *TBX5^{in/del}* path. Activation of *WNT2* and *NKX2-5* in the
601 deduced *TBX5^{in/del}* path was delayed. Significance was determined by Wilcoxon Rank Sum test
602 (adj p-value < 0.05).
603
604

Figure 4



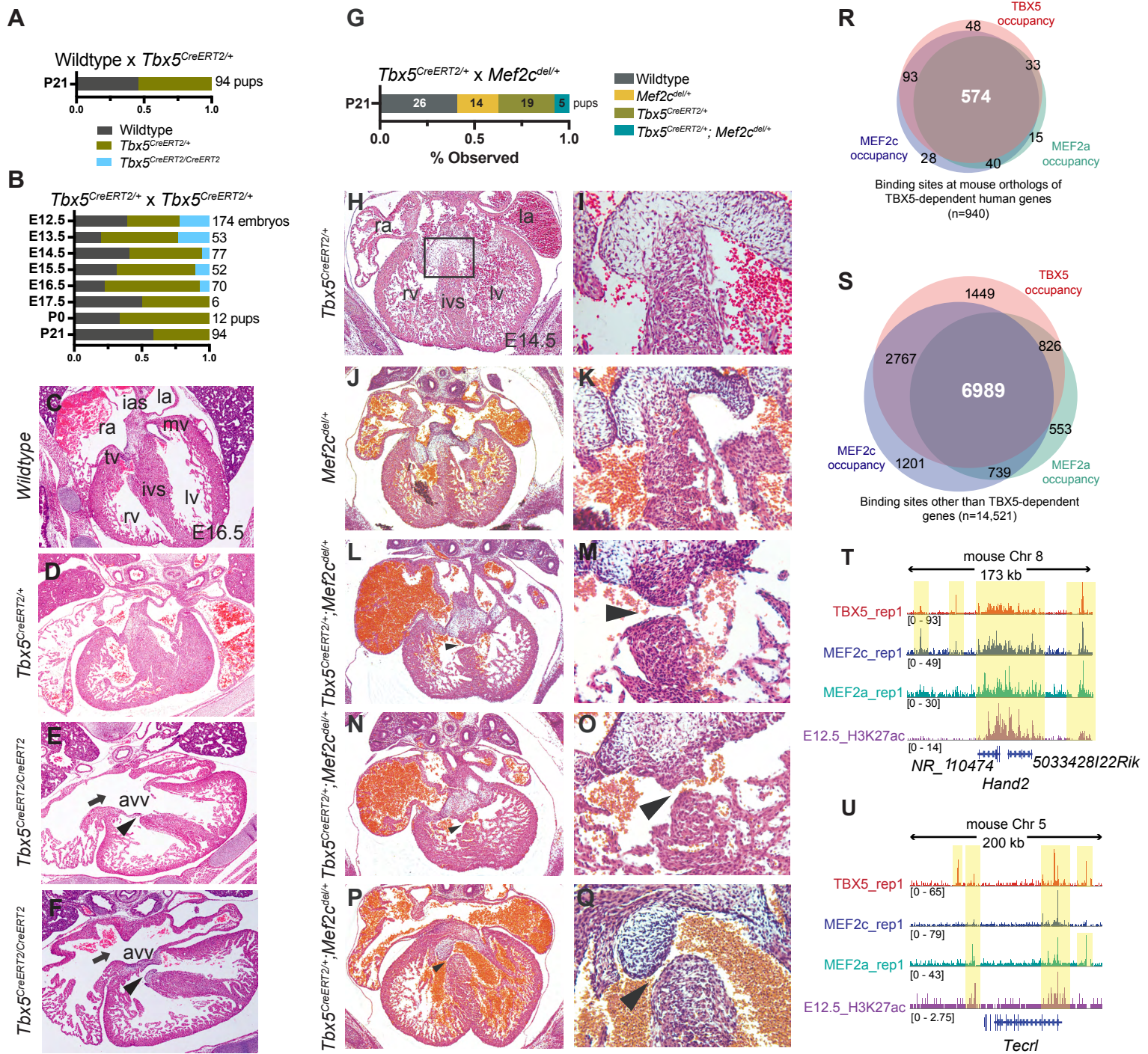
605 **Figure 4. Subsets of cardiomyocytes respond discretely by quantitative transcriptional**
606 **perturbations to reduced TBX5 dosage.** (A-B) *TNNT2*⁺ clusters from day 23 were re-clustered
607 in Seurat. UMAP shows cells colored by biological replicate (A) or *TBX5* genotype (B). (C) *TBX5*
608 genotype-dominant clusters segregated at low resolution of Louvain clustering. (D) Clusters
609 enriched for WT or *TBX5*^{in/+} were compared by differential gene expression. Top five
610 upregulated or downregulated genes are displayed. EP (orange) or CHD (purple) genes are
611 shown. Transcriptional regulators are denoted by asterisks, and predicted targets of *TBX5*,
612 based on *TBX5* occupancy (Ang et al., 2016) are bolded (Table S4). Dot size corresponds to
613 the percentage of cells expressing the gene in a cluster, while the color intensity represents
614 scaled expression values in a cluster. Significance was determined by Wilcoxon Rank Sum test
615 (adj p-value<0.05). (E) Clusters enriched for WT or *TBX5*^{in/del} were compared by differential
616 gene expression. (F) Common genes that were differentially expressed between WT- vs.
617 *TBX5*^{in/+}-enriched clusters and WT vs. *TBX5*^{in/del}-enriched clusters are shown. (G) Fluorescence
618 *in situ* hybridization is visualized for *TNNT2* (green) or *NPPA* (red) in day 23 cardiomyocytes,
619 from WTC11, control, *TBX5*^{in/+}, *TBX5*^{in/del} and *TBX5*^{PuR/PuR} cells. Brightness and contrast of
620 images have been adjusted to facilitate viewing of cells. (H) Graph displays mean intensity of
621 *NPPA* signal of individual double-positive *TNNT2*⁺/*NPPA*⁺ cells by *TBX5* genotype. Significance
622 of p-values were calculated by unpaired *t* test. (I-K) Pseudocolor plots of flow cytometry show
623 cTNT⁺ or DES⁺ cells in (I) wildtype, (J) *TBX5*^{in/+} or (K) *TBX5*^{in/del} at day 23. The number of
624 double-positive cTNT⁺/DES⁺ cells are significantly different between wildtype and *TBX5*^{in/+} and
625 between wildtype and *TBX5*^{in/del} (p-value<1E-4 by Chi-Square test). (L) UMAP shows cells
626 colored by cluster at higher resolution of Louvain clustering, indicating putative *TNNT2*⁺ subsets.
627 (M) A phylogenetic tree shows the relatedness of the 'average' cell in each cluster using PC
628 space. The proportion of cells in each cluster are colored by *TBX5* genotype. Related clusters
629 between different *TBX5* genotypes were selected for differential gene tests. (N) Heatmap shows
630 hierarchically-sorted enriched genes in clusters 6 or 10, which consists of each *TBX5* genotype.
631 (O) UMAP displays combined WT-enriched (black) or *TBX5*^{in/del}-enriched (blue) clusters for
632 comparison. (P) Dot plots show top five differentially expressed upregulated or downregulated
633 genes, along with EP or CHD genes, between aggregate WT-enriched and *TBX5*^{in/del}-enriched
634 clusters. (Q, S, U) UMAPs highlight clusters used for pair-wise comparisons for differential gene
635 tests in corresponding dot plots below. (R, T, V) Dot plots of top differentially expressed genes
636 between WT/*TBX5*^{in/+}-enriched cluster 5 and *TBX5*^{in/+}-enriched cluster 7 (R), between WT-
637 enriched cluster 1 and *TBX5*^{in/+}-enriched cluster 2, or (V) between WT-enriched cluster 14 and
638 *TBX5*^{in/+}-enriched cluster 11. A few differentially expressed genes are common between
639 comparisons in (R) and (T). Total number of differentially expressed genes for each comparison
640 is listed (Table S2).
641
642

Figure 5



643 **Figure 5. TBX5 dosage preserves cardiomyocyte network stability.** (A, B) Gene regulatory
644 networks (GRNs) of *TNNT2*⁺ cells for each *TBX5* genotype at day 6, 11, or 23 were inferred.
645 GRNs at day 11 for WTC11 (A) or *TBX5*^{in/+} (B) are shown. Nodes of CHD (purple), heart
646 development (red) or electrophysiology (orange) genes are shown. The size of each node
647 represents the quantitative importance of the gene, based on pagerank centrality. Note the
648 absence of *SMAD2* and the reduced centrality of *MEF2C* (smaller circle) in the *TBX5*^{in/+} network,
649 compared to WTC11. (C) Pagerank centrality for significantly altered (top 5% cutoff) nodes of
650 CHD, heart development or EP genes at specific time points are shown. Twenty CHD genes
651 display a reduction in pagerank (top 5% cutoff, when compared to wildtype and control) in at
652 least one *TBX5* mutant genotype at any stage. This indicates enrichment of CHD genes in
653 *TBX5* dosage-sensitive networks ($p < 2.2 \times 10^{-5}$ by hypergeometric test). (D) *TBX5*-dependent
654 genes with a reduction of pagerank are correlated (correlation > 0.5), anti-correlated (correlation
655 < -0.5), or indeterminate ($0.5 < \text{correlation} < -0.5$) with *TBX5* expression in *TNNT2*⁺ cells. (E)
656 Degree centrality for *MEF2C* is reduced in *TBX5*^{in/del} at day 6 and reduced in *TBX5*^{in/+} and
657 *TBX5*^{in/del} at day 11 (top 5% cutoff, when compared to wildtype and control), but not at day 23.
658 (F) Correlations with *MEF2C* and *TBX5*-dependent genes with a reduction of degree centrality
659 in *TNNT2*⁺ cells are plotted. Additional data can be found in Table S6.
660
661

Figure 6



662 **Figure 6. *Tbx5* and *Mef2c* cooperate in heart development.** (A) Pups at postnatal day 21
663 (P21) from matings of wildtype X *Tbx5*^{CreERT2/+} were genotyped, and expected Mendelian ratios
664 were observed. (B) Expected Mendelian ratios from *Tbx5*^{CreERT2/+} X *Tbx5*^{CreERT2/+} were not
665 observed for *Tbx5*^{CreERT2/CreERT2} embryos after embryonic day 13.5 (E13.5), and none were
666 recovered beyond E16.5. (C-F) Transverse sections of hearts at E16.5 from each *Tbx5*
667 genotype are shown. In *Tbx5*^{CreERT2/CreERT2} embryos, note atrioventricular canal defects,
668 consisting of atrioventricular valves (AVV), ventricular septal defects (arrowhead), and atrial
669 septal defects (arrow). LV, left ventricle; RV, right ventricle; IVS, interventricular septum; LA, left
670 atrium; RA, right atrium; IAS, interatrial septum. (G) Pups at P21 from matings of *Tbx5*^{CreERT2/+} X
671 *Mef2c*^{del/+} were genotyped. Expected Mendelian ratios were not observed for
672 *Tbx5*^{CreERT2/+}; *Mef2c*^{del/+} at P21. (H, J, L, N, P) Transverse sections of hearts at embryonic day
673 14.5 (E14.5) from each genotype are shown. (I, K, M, O, Q) Magnified views of the
674 interventricular septum are shown. In *Tbx5*^{CreERT2/+}; *Mef2c*^{del/+} embryos, VSDs are observed,
675 including muscular VSDs (arrowheads in M, O), a subaortic membranous VSD (Q, arrowhead)
676 and dilated blood-filled atria (L, N, P). (R, S) Venn diagrams display the overlap of TBX5,
677 MEF2a or MEF2c occupancy near mouse orthologs of human TBX5-dependent (R) or -
678 independent genes (S). (T, U) Browser tracks for ChIP-seq data from E12.5 hearts for TBX5,
679 MEF2c, MEF2a and H3K27ac near TBX5-dependent genes, *Hand2* (T) or *Tecrl* (U). Yellow
680 bands of shading indicate co-occupancy. Table S7 displays odds ratios (FDR<0.05) of TBX5,
681 MEF2a or MEF2c occupancy near human TBX5-dependent genes, while Table S8 displays
682 odds ratio (FDR<0.05) of co-occupancy of TBX5, MEF2a and MEF2c near mouse orthologs of
683 TBX5-dependent human genes.
684
685
686

687 **METHODS**

688 **CONTACT FOR REAGENT AND RESOURCE SHARING.** All unique/stable reagents
689 generated in this study are available from the Lead Contact, Benoit Bruneau
690 (benoit.bruneau@gladsatone.ucsf.edu) with a completed Materials Transfer Agreement.

691

692 **EXPERIMENTAL MODEL AND SUBJECT DETAILS**

693 **Gene targeting and genotyping of human iPS cells mutant for *TBX5*.** sgRNAs for *TBX5*
694 exon 3 (sgRNA1, TCCTTCTTGCAGGGCATGGA) or exon 7 (sgRNA2,
695 CCTTTGCCAAAGGATTTTCG), which encode the T-box domain, were selected using
696 crispr.genome-engineering.org, and cloned by annealing pairs of oligos into a plasmid
697 containing humanized *S. pyogenes* Cas9, as described in (Cong et al., 2013) (px330-U6-
698 Chimeric_BB-CBh-hSpCas9 was a gift from Feng Zhang, Addgene #42230).

699 For WTC11-derivatives *TBX5*^{+/+} (control), *TBX5*^{in/+} or *TBX5*^{in/del}, the induced pluripotent
700 stem (iPS) cell line WTC11 (gift from Bruce Conklin, available at NIGMS Human Genetic Cell
701 Repository/Coriell #GM25236) (Miyaoaka et al., 2014) was electroporated (Lonza #VPH-5012)
702 with a cloned nuclease construct containing a guide RNA (sgRNA1) targeting exon 3 of *TBX5*,
703 as described in (Mandegar et al., 2016; Miyaoaka et al., 2014). Cells were plated on human ESC-
704 grade Matrigel (Corning #354277) and cultured in mTeSR-1 (StemCell Technologies Cat
705 #05850) with 10μM ROCK inhibitor (StemCell Technologies, Y-27632). For screening of *TBX5*
706 exon 3 non-homologous end-joining (NHEJ) mutations, genomic DNA flanking the targeted
707 sequence was amplified by PCR (For1: ATGGCATCAGGCGTGCCTATAA and Rev1:
708 CCCACTTCGTGGAATTTTAGCCA), amplicons underwent digestion by NlaIII, and then were
709 evaluated for loss of NlaIII by gel electrophoresis (wildtype band 800bp, mutant band 880bp).
710 Clones with no change, a heterozygous or homozygous loss of NlaIII were sequenced (For1:
711 ATGGCATCAGGCGTGCCTATAA, Rev1: TTCCGGGCTTGA ACTTCTGG, Seq1:
712 ATAGCCTTGTGCTGATGGCA).

713 For generation of $TBX5^{PuR/PuR}$, a puromycin resistance gene cassette (Frt-PGK-EM7-
714 PuroR-bpA-Frt) containing homology arms of 469bp (5' homology arm) and 466bp (3'
715 homology arm) around the sgRNA1 target site at +9bp from the start of $TBX5$ exon 3 was
716 cloned by Cold Fusion (System Biosciences #MC010B) using amplicons from genomic DNA of
717 WTC11 into a construct that was a modification of plasmid pEN114 (Nora et al., 2017). WTC11
718 cells were electroporated with a cloned nuclease construct containing a guide RNA targeting
719 exon 3, along with the $TBX5$ exon3 homology arm-Frt-PGK-EM7-PuroR-bpA-Frt cassette and
720 plated as a serial dilution in mTeSR-1 with Rock inhibitor, as described in (Mandegar et al.,
721 2016). On day 2 and subsequent days, cells were grown in media containing mTeSR-1, Rock
722 inhibitor and puromycin (0.5ug/mL), to select for puromycin-resistant cells. For screening of
723 $TBX5$ exon 3 homology-directed repair (HDR) mutations, genomic DNA flanking the targeted
724 sequence was amplified by PCR (For1: ATGGCATCAGGCGTGCCTATAA, and Rev2:
725 CCCACTTCGTGGAATTTTAGCCA for wildtype, 797 bp, For1:
726 ATGGCATCAGGCGTGCCTATAA, Rev3: GTTCTTGCAGCTCGGTGAC (Nora et al., 2017) for
727 PuroR, 1631 bp). Positive 5' arm clones were genotyped by PCR for the 3' arm (For2:
728 ATTGCATCGCATTGTCTGAG (Nora et al., 2017), Rev4: TTTGACAATCGGGTGGGACC, 829
729 bp).

730 For PGP1-derivatives $TBX5^{in/+}$ or $TBX5^{del/del}$, the iPS cell line PGP1 (gift from George
731 Church, available at NIGMS Human Genetic Cell Repository/Coriell #GM23338) (Lee et al.,
732 2009) was electroporated with a cloned nuclease construct containing a guide RNA (sgRNA2)
733 targeting exon 7 of $TBX5$, as described in (Byrne and Church, 2015). For screening of $TBX5$
734 exon 7 NHEJ mutations, the targeted sequence was amplified using PCR primers (For3:
735 GCTTCTTTTGGTTGCCAGAG, Rev5: CATTCTCCCCATTTCCATGT, Seq2:
736 AGAGGCTGCATTTCCATGAT), Illumina compatible-libraries from clones were generated and

737 multiplex-sequenced on a MiSeq for purity of homogeneity of clones for heterozygous or
738 homozygous mutations, as described in (Byrne and Church, 2015).
739
740 **Isolation of homogenous iPS cell clones.** Isolation of homogenous colonies for WTC11-
741 derivatives *TBX5*^{+/+} (control), *TBX5*^{in/+} or *TBX5*^{in/del} was performed by modification of methods
742 described previously (Mandegar et al., 2016; Peters et al., 2008). Briefly, single cell suspension
743 of electroporated iPS cells was plated on Matrigel-coated 6 well plates (WP) (BD Bioscience
744 #351146). Once cultures were adherent and recovered to ~80% confluency, cells were
745 detached by Accutase Cell Detachment Solution (Stemcell Technologies #07920), diluted with
746 1X DPBS without Ca²⁺/Mg²⁺ and singularized using a P1000 filtered tip, and centrifuged. The
747 cell pellet was resuspended in mTeSR-1, Rock inhibitor and Gentamicin (Life Technologies
748 #15750-060) media, incubated with DAPI (1:1000 from a 1mg/mL stock) for 5 min, centrifuged
749 and resuspended at a concentration of at least 1.0E6 cells/mL in mTeSR-1, Rock inhibitor and
750 Gentamicin media without DAPI. After filtering cells with a 40-micron mesh into FACS tubes,
751 remaining cells (about 120,000 cells per well) were plated onto 6WP for maintenance. Single
752 cells were then sorted for DAPI negativity using a BD FACS AriaII or AriaIII, with a 100-micron
753 nozzle at the lowest flow rate available, into individual wells of a 96WP coated with Matrigel
754 containing media of mTeSR-1, Rock inhibitor and Gentamicin. Upon recovery at 37°C, each well
755 was evaluated one day later for no cells, one cell or more than one cell. All cells were
756 maintained with mTeSR-1, Rock inhibitor and Gentamicin media for at least 5 days, then with
757 mTeSR-1 alone for an additional 5-7 days. Each well at 25% confluency was harvested and re-
758 plated upon singularization with P200 tips in 96WP for more efficient cell growth. When the cell
759 confluency of each well from “single” cells was nearly 100%, then 90% of cells were harvested
760 for genotyping using QuickExtract DNA lysis solution (Epicentre #QE0905T), while 10% of cells
761 were re-plated for the next round of cell selection for wells of interest by FACS sorting again or
762 by serial dilution of cells for manual picking of colonies, as described in (Mandegar et al., 2016;

763 Miyaoka et al., 2014) from apparent “single” cells. Rounds were repeated until every daughter
764 well showed the same genotype, consistent with homogeneity. Genomic DNA from individual
765 wells of interest were amplified using high fidelity *Taq* polymerase, TA-cloned and sequenced to
766 confirm genotype and homogeneity.

767 Isolation of homogenous colonies for PGP1-derivatives *TBX5^{in/+}* or *TBX5^{del/del}* was
768 performed as described in (Byrne and Church, 2015). Isolation of homogenous colonies for
769 WTC11-derivative *TBX5^{PuR/PuR}* was performed as described in (Mandegar et al., 2016). After
770 sequencing confirmation of respective genotypes, karyotypically-normal cells from each iPS cell
771 line were expanded for subsequent studies.

772

773 **Mice.** All mouse protocols were approved by the Institutional Animal Care and Use Committee
774 at UCSF. *Tbx5^{del/+}* (Bruneau et al., 2001) and *Tbx5^{CreERT2IRES2xFLAG}* (abbreviated here as
775 *Tbx5^{CreERT2}*) (Devine et al., 2014b) mice were described previously. *Mef2c^{del/+}* mice (Lin et al.,
776 1997) were obtained from Brian Black. *Tbx5^{CreERT2/+}* and *Mef2c^{del/+}* were maintained in the
777 C57BL6/J background (Jackson Laboratory #664). *Tbx5^{fl-bio/fl-bio}* (Waldron et al., 2016) mice were
778 obtained from Frank Conlon. *Mef2a^{fl-bio}* and *Mef2c^{fl-bio}* (Jackson Laboratory #025983) were
779 described in (Akerberg et al., 2019). *Rosa26BirA* mice were obtained from the Jackson
780 Laboratory (#010920) (Driegen et al., 2005).

781

782 **METHOD DETAILS**

783 **Maintenance of iPS cells and differentiation to cardiomyocytes.** All iPS cell lines were
784 transitioned to and maintained on growth factor-reduced basement membrane matrix Matrigel
785 (Corning #356231) in mTeSR-1 medium. For directed cardiomyocyte differentiations, iPS cells
786 were dissociated using Accutase and seeded onto 6WP or 12WP. The culture was allowed to
787 reach 80-90% confluency and induced with the Stemdiff Cardiomyocyte Differentiation Kit
788 (Stemcell Technologies #05010), according to the manufacturer’s instructions. Starting on day

789 7, differentiations were monitored daily for beating cardiomyocytes and onset of beating was
790 recorded as the day when beating was first observed.

791

792 **Flow Cytometry.** iPS-derived cardiomyocytes from WTC11, Control, *TBX5^{in/+}* and *TBX5^{in/del}*
793 lines were dissociated using Trypsin-EDTA 0.25% on day 15 or day 23 after induction of the
794 differentiation protocol and fixed with 4% methanol-free formaldehyde. Cells were washed with
795 PBS and permeabilized using FACS buffer (0.5% w/v saponin, 4% Fetal Bovine Serum in PBS).
796 For evaluation of differentiation efficiency, cells were stained with a mouse monoclonal antibody
797 for cardiac isoform Ab-1 Troponin at 1:100 dilution (ThermoFisher Scientific #MS-295-P) or the
798 isotype control antibody (ThermoFisher Scientific #14-4714-82). For analyzing levels of Desmin
799 protein, cells were co-stained with the mouse monoclonal antibody for cardiac isoform Ab-1
800 Troponin at 1:100 dilution and recombinant rabbit anti-Desmin antibody at 1:70 dilution (Abcam
801 #ab32362), or normal rabbit IgG antibody (Millipore Sigma #NI01) for 1 hour at room
802 temperature. After washing with FACS buffer, cells were stained with the following secondary
803 antibodies - goat anti-mouse IgG Alexa 594 at 1:200 dilution (ThermoFisher Scientific #A-
804 11005) and donkey anti-rabbit IgG Alexa 488 at 1:200 dilution (ThermoFisher Scientific
805 #A21206) for 1 hour at room temperature. Cells were then washed with FACS buffer, stained
806 with DAPI for 5 minutes, rinsed, and filtered with a 40-micron mesh. At least 10,000 cells were
807 analyzed using the BD FACSAriaII or AriaIII (BD Bioscience), and results were processed using
808 FlowJo (FlowJo, LLC).

809

810 **Western blotting.** iPS-derived cardiomyocytes were harvested on day 15, pelleted and flash
811 frozen. Protein was isolated from supernatant in RIPA buffer with EDTA-free protease and
812 phosphatase inhibitor (ThermoFisher Scientific) after sonication (15 second pulse on, 15 second
813 pulse off, for four pulses). After quantification by BCA assay (ThermoFisher Scientific), 150µg of
814 total protein was loaded per well for each genotype. After running on SDS-PAGE and wet

815 transfer with NuPage Transfer buffer (ThermoFisher Scientific) to a PVDF membrane, the blot
816 was washed in PBST and incubated in primary antibodies of rabbit polyclonal anti-TBX5 at a
817 1:400 dilution (Sigma #HPA008786) and mouse monoclonal anti-cTNT at 1:1000 dilution
818 (ThermoFisher Scientific #MS-295-P), followed by secondary antibody incubation with donkey
819 anti-rabbit IgG IRDye680 at 1:2000 dilution (Licor #926-68073) and donkey anti-mouse IgG
820 IRDye800 at 1:2000 dilution (Licor #926-32212). The blot was imaged on an Odyssey FC Dual-
821 Mode Imaging system (Licor).

822

823 **Fluorescent *in situ* hybridization.** iPS cell-derived cardiomyocytes from WTC11, Control,
824 $TBX5^{in/+}$, $TBX5^{in/del}$ and $TBX5^{PuR/PuR}$ were dissociated using Trypsin-EDTA 0.25% on day 23 after
825 induction of the differentiation protocol, and 25,000-40,000 cells were plated on to 8-well
826 chambered slides (Ibidi #80826), to obtain a relatively sparse monolayer of cardiomyocytes.
827 Cells were fixed the following day with 10% Neutral Buffered Formalin for 15 minutes at room
828 temperature. Cells were then serially dehydrated in 50%, 70% and 100% ethanol and stored at -
829 20°C until ready to be hybridized. *In situ* hybridization was performed using the RNAscope
830 Multiplex Fluorescent v2 Assay kit (Advanced Cell Diagnostics #323100) with probes for *Hs-*
831 *TNNT2* (#518991) and *Hs-NPPA* (#531281). Slides were imaged at 10X and 40X magnification
832 on the Keyence BZ-X710 All-in-One Fluorescence Microscope. Non-saturated mean intensity of
833 *NPPA* signal was measured in each *TNNT2*+ cell from every group. Unpaired t-tests were used
834 to calculate statistical significance. Brightness and contrast of images in Figure 4N have been
835 adjusted to facilitate viewing of cells.

836

837 **Replating cardiomyocytes for single cell electrophysiology.** iPS cell-derived
838 cardiomyocytes (day 15 or older) from WTC11, Control, $TBX5^{in/+}$, $TBX5^{in/del}$ and $TBX5^{PuR/PuR}$
839 were gently dissociated in Trypsin-EDTA 0.25% and quenched using StemDiff Maintenance
840 Medium with 10% FBS. Cell suspension was centrifuged at 800 rpm for 5 minutes. The pellet

841 was resuspended in StemDiff Maintenance Medium with Rock inhibitor at a 1:1000 dilution.
842 Cardiomyocytes were counted, and 25,000-35,000 cells were plated on to growth factor-
843 reduced Matrigel-coated 15mm round glass coverslips (Warner Instruments #64-0703) to obtain
844 a sparse distribution. Cardiomyocytes were then maintained on coverslips in StemDiff
845 Maintenance Medium.

846

847 **Patch Clamp Electrophysiology.** Patch clamp recordings were made on single iPSC-derived
848 cardiomyocytes using the perforated-patch configuration. Experiments were performed at 30°C
849 under continuous perfusion of warmed Tyrode's solution containing (in mM): 140 NaCl, 5.4 KCl,
850 1 CaCl₂, 1 MgCl₂, 10 glucose, and 10 HEPES, with the pH adjusted to 7.4 with NaOH.

851 Recordings were conducted using borosilicate glass pipettes (Sutter Instruments) with typical
852 resistances of 2 to 4MW. The pipette solution consisted of (in mM): 150 KCl, 5 NaCl, 5 MgATP,
853 10 HEPES, 5 EGTA, 2 CaCl₂, and 240 mg/mL amphotericin B, with the pH adjusted to 7.2 with
854 KOH. Spontaneous action potentials were acquired in a zero-current current clamp
855 configuration using an Axopatch 200B amplifier and pClamp 10 software (Axon Instruments).
856 Data was digitized at 20 kHz and filtered at 1kHz. Action potential parameters from each cell
857 were derived using Clampfit 10 software (Axon Instruments).

858

859 **Calcium imaging.** iPSC-derived cardiomyocytes on glass coverslips were loaded with Ca²⁺
860 indicator dye Fluo-4 AM (Thermo Fisher Scientific #F14201) to record Ca²⁺ flux, as previously
861 described (Spencer et al., 2014). Measurements were made on spontaneously firing single or
862 small clusters of iPSC-derived cardiomyocytes using a 10X objective on a Zeiss Axio Observer
863 Z1 inverted microscope. For experiments, cells were placed in Tyrode's solution containing 1.8
864 mM Ca²⁺ within a 37°C heated stage-top imaging chamber (Okolab). Images were acquired at
865 100 fps using an ORCA-Flash 4.0 camera (Hamamatsu, Bridgewater, NJ). Data was processed

866 using ZEN (Zeiss) or Image J software (<http://rsbweb.nih.gov/ij/>) and analyzed using custom in-
867 house software (Hookway et al., 2019).

868

869 **Immunostaining of cardiomyocytes.** iPSC-derived cardiomyocytes from WTC11, Control,
870 $TBX5^{in/+}$ and $TBX5^{in/del}$ were replated on coverslips placed in 12-well plates on day 23, as
871 described above for replating for electrophysiology. Cells were fixed in 4% formaldehyde for 20
872 minutes at room temperature, followed by washes in PBS. Cells were then treated with a
873 blocking buffer containing 5% goat serum and 0.1% Triton X-100 in PBS for 1 hour at room
874 temperature. A mouse monoclonal antibody for cardiac isoform Ab-1 Troponin (ThermoFisher
875 Scientific #MS-295-P) was added to the coverslip-containing wells at a 1:100 dilution in blocking
876 buffer and incubated on a rocker for 2 hours at room temperature. Following washes with 0.1%
877 Triton X-100 in PBS, coverslips were treated with a donkey anti-rabbit IgG Alexa 488 antibody
878 (ThermoFisher Scientific #A21206) at a 1:200 dilution for 2 hours at room temperature.
879 Coverslips were then washed with 0.1% Triton X-100 in PBS and stained with DAPI at a 1:1000
880 dilution for 2 minutes. Coverslips were washed and stored in PBS at 4C. Images were acquired
881 on a Zeiss LSM 880 with Airyscan and processed by ImageJ (Abràmoff et al., 2004).

882

883 **Cell harvesting for single cell RNA sequencing.** Cells from day 6, day 11 or day 23 of the
884 differentiation protocol were collected from 3 independent differentiations. Wells for dissociation
885 were chosen based on typical differentiated morphology on day 6 or robust beating on day 11
886 and day 23. Cells were singularized with Trypsin-EDTA 0.25%. After quenching, the single cell
887 suspension was centrifuged at 800 rpm for 5 minutes. The pellet was resuspended in 1X PBS
888 with 0.04% w/v Ultrapure BSA (MCLAB #UBSA-500) and counted. A 30 μ L cell suspension
889 containing 10,000 cells was used to generate single cell droplet libraries with the Chromium
890 Single Cell 3' GEM, Library & Gel Bead Kit v2 according to manufacturer's instructions (10X
891 Genomics). After KAPA qPCR quantification, a shallow sequencing run was performed on a

892 NextSeq 500 (Illumina) prior to deep sequencing on a NextSeq 500, HiSeq 4000, or NovaSeq
893 (Illumina) for a read depth of >100 million reads per cell.

894

895 **Data processing using Cellranger.** All datasets were processed using Cellranger 2.0.2.

896 FASTQ files were generated using the mkfastq function. Reads were aligned to hg19 reference
897 (version 1.2.0). Cellranger aggr was used to aggregate multiple GEM libraries.

898

899 **Seurat analysis.** Outputs from the Cellranger pipeline were analyzed using the Seurat package
900 (version 2.3.4 or 3.1.4) (Butler et al., 2018; Satija et al., 2015; Stuart et al., 2019) in R (version
901 3.5.1) [R Core Team (2018). R: A language and environment for statistical computing. R
902 Foundation for Statistical Computing, Vienna, Austria. URL <https://www.R-project.org/>].

903 Datasets from day 6, day 11 or day 23 experiments were analyzed as separate Seurat objects.

904 Seurat objects for day 6 or day 11 were generated using Seurat v2. Seurat objects for day 23
905 datasets with multiple biological replicates were generated using Seurat v3, unless otherwise
906 noted.

907 Quality control steps were performed to remove dead cells or doublets, and cells with a
908 UMI count between 10,000 to 80,000 were retained. After normalizing the data, sources of
909 unwanted variation, such as differences in the number of UMI, number of genes, percentage of
910 mitochondrial reads and differences between G2M and S phase scores were regressed using
911 the ScaleData function. Next, principal component analysis (PCA) was performed using the
912 most highly variable genes. Cells were then clustered based on the top 25-30 principal
913 components and visualized using a dimensionality reduction method called Uniform Manifold
914 Approximation and Projection (UMAP) (Becht et al., 2018). The resolution parameter was set,
915 so that cluster boundaries largely separated the likely major cell types.

916 Two technical replicates at day 6 and day 11 for WTC11-derived cells (WTC11, control,
917 *TBX5^{in/+}*, *TBX5^{in/del}*) were evaluated. For control at day 23, two technical replicates were

918 evaluated. For WTC11, *TBX5^{in/+}* or *TBX5^{in/del}* at day 23, two technical replicates from biological
919 replicate 1 and one sample from biological replicate 2 were evaluated. For PGP1-derived cells
920 (PGP1, *TBX5^{in/+}* and *TBX5^{del/del}*), one sample for each genotype was evaluated.

921 Major cell type categories were defined by their expression of select enriched genes in a
922 given cluster--pluripotent cells (*POU5F1*) cardiomyocytes (*TNNT2*), dividing cardiomyocytes
923 (*CENPF⁺/TNNT2⁺*), ventricular cardiomyocytes (*TNNT2⁺/IRX4⁺*), fibroblasts (*COL1A1*),
924 epicardial cells (*WT1⁺/TBX18⁺*), neural crest-derived cells (*MAFB⁺, MSX1⁺*), endoderm (*TTR*
925 alone or *TTR⁺/AFP⁺*) and endothelial cells (*PLVAP*). Clusters of cells not defined by any of these
926 markers were labeled as “Undetermined”. The numbers of cells in each major cell type category
927 in each genotype were then calculated. Sunburst plot was generated in Excel using the
928 percentage of cells in each cell type category per genotype. We used FindAllMarkers to
929 generate a list of top marker genes for each cluster and highlighted selected genes in a
930 Manhattan plot to display potential diversity of subtypes among these major cell types.

931

932 **Integration and Visualization of Datasets from Multiple Samples.** For the day 23 WTC11-
933 derived cell line (biological replicate 1 and 2) analysis, we ran CellRanger to normalize
934 sequencing depth variation between individual libraries. We then ran Seurat v3.1.4’s ‘Integration
935 and Label Transfer-SCTransform’ workflow to resolve effects from experimental instances that
936 are driven by cell-cell technical variations, including sequencing depth (Hafemeister and Satija,
937 2019; Stuart et al., 2019). Cells with lower than 10,000 UMIs and concurrently higher
938 percentage of mitochondrial reads were removed. Potential doublets with higher than 75,000
939 UMIs were also removed. The dataset was then split into two Seurat objects using the biological
940 replicate status. We ran CellCycleScoring(default) and
941 SCTransform(vars.to.regress=c(“S.Score”, “G2M.Score”)) to regress out cell cycle variations.
942 The remaining steps followed the ‘Integration and Label Transfer-SCTransform’ workflow.
943 Briefly, these steps include finding 2,000 highly variable genes to create anchors that represent

944 biologically common cells connected from opposing batches. After integration, Seurat set the
945 active assay to 'integrated' for downstream data visualization analysis. UMAPs were created by
946 running RunPCA(default) and RunUMAP(default).

947 We also evaluated genetic backgrounds from two iPSC lines. The WTC11-derived cell
948 lines were considered genetic background 1, which included biological replicate 1 and 2. PGP1-
949 derived cell lines were considered genetic background 2. We followed the same CellRanger
950 aggregate and qc filtering. However, we used the genetic background status to make three
951 Seurat objects and no variables were regressed when running the 'Integration and Label
952 Transfer-SCTransform' workflow. UMAPs were created by running RunICA(default) and
953 RunUMAP(reduction="ica", dims=1:40, min.dist=0.4, spread=0.9, repulsion.strength=6).

954 For day 23 cardiomyocyte datasets, *TNNT2*⁺ clusters were defined as containing a
955 majority of cells expressing *TNNT2* on a feature plot and extracted using the subset function
956 and re-clustered. Subsequently, the resolution parameter was set to partition clusters enriched
957 for a particular genotype. A phylogenetic tree was generated by relating the "average" cell from
958 each cluster in PC space, using the BuildClusterTree function. Differential gene expression tests
959 were run between closely related clusters, using the FindMarkers function with min.pct set to 0.1
960 and logfc.threshold set to 0.25. Selected differentially expressed genes with an adjusted p-value
961 less than 0.05 from the Wilcoxon Rank Sum test were then displayed using the Dotplot function.
962 As Seurat log normalizes gene expression counts and scales values for each gene (mean is 0,
963 std dev of +/-1), dot plots and heatmaps are based on scaled expression values.

964

965 **Cell Type Classifier by Machine Learning.** We applied machine learning to predict
966 corresponding *in vivo* cell types in our WTC11-derived samples. A sklearn multiclass logistic
967 regression model, using a one-vs-rest scheme and the cross-entropy loss cost function
968 (Pedregosa et al., 2011), was trained on the *in vivo* scRNA-seq dataset published by (Asp et al.,
969 2019). The training data contained eleven cardiac cell type classes (i.e. Fibroblast-like, atrial

970 cardiomyocyte (aCM)-like, ventricular cardiomyocyte (vCM)-like, Cardiac neural crest-like, Sub-
971 epicardial-like, Capillary endothelium/pericytes/adventitia-like, Smooth muscle/fibroblast-like,
972 and Erythrocyte-like). The test data was the day 23 integrated WTC11-biological replicates.

973 We ran SCTransform(default) independently on the training and test data to remove
974 sequencing depth bias, while preserving biological heterogeneity. To train our classifier on cell-
975 type specific signals from both datasets, we used SCTransform Pearson residuals as the
976 feature space for 1,538 genes. The genes were selected by taking the intersection of the top
977 3,000 highly variable genes (HVGs) from the training and test datasets (Table S1).

978 We evaluated the cell type classifier using sklearn's stratified 10-fold cross validation
979 method; StratifiedKFold(n_splits=10, random_state=42). Each fold preserves the
980 percentage of *in vivo* cell types. Thus, recapitulating true *in vivo* cardiac cell type
981 composition in our training evaluation. For each fold of the cross validation, we used a
982 sklearn logistic regression model to fit and predict on the fold's training and test set;
983 LogisticRegression(penalty='l2', solver='lbfgs', random_state=42). The cross validation
984 model's average performance measurements were: accuracy (96.9%), precision (97.8%),
985 recall (97.4%), and f1 score (97.1%) (Figure S2C). Due to the strong cross validation
986 performance, we trained our deployment model on the full *in vivo* dataset to increase cell
987 type generalisability. The trained multinomial classifier was then deployed on our WTC11-
988 derived samples.

989

990 **Congenital Heart Disease-Associated or Electrophysiology-Related Gene Lists and Cell**

991 **Type Expression.** A list of 375 CHD candidate genes, including inherited, *de novo*, syndromic
992 or non-syndromic CHD genes of interest, was manually curated from literature (Homsy et al.,
993 2015; Jin et al., 2017; Lalani and Belmont, 2014; McCulley and Black, 2012; Prendiville et al.,
994 2014; Priest et al., 2016; Sifrim et al., 2016; Zaidi et al., 2013). A list of 76 EP genes were

995 manually curated. A list of cardiac development-related factors is from (Duan et al., 2019). Lists
996 can be found in Table S3.

997

998 **Cell trajectories and pseudotime analysis.** Pseudotime analysis was performed using the
999 URD package (version 1.0.2) (Farrell et al., 2018b). A single Seurat object (from Seurat v2),
1000 consisting of combined data from two technical replicates of three timepoints and four
1001 genotypes, was processed as described in the previous section, and then converted to an URD
1002 object using the `seuratToURD` function. Cell-to-cell transition probabilities were constructed by
1003 setting the number of nearest neighbors (`knn`) to 211 and `sigma` to 8. Pseudotime was then
1004 calculated by running 80 flood simulations with *POU5F1*⁺ clusters as the 'root' cells. Next, all
1005 day 23 clusters were set as 'tip' cells and biased random walks were simulated from each tip to
1006 build an URD tree.

1007 We identified URD monotonic genes, which are genes that neither deviate from an
1008 increase or decrease in expression with pseudotime. Spearman rank correlation (Python v3.7.3,
1009 and libraries Pandas 0.25.0, Numpy 1.17.1, and SciPy 1.3.1) was used to find significant
1010 monotonic genes (p -value < 0.05). To determine if these monotonic relationships differ between
1011 WT and *TBX5*^{in/del} paths to cardiomyocytes, we used a Fisher z-transformation to test the null
1012 hypothesis that there is no significant difference in correlation (Fisher, 1921). To illustrate these
1013 results, we use heatmaps for genes with a $|\rho| \geq 0.4$ to pseudotime and Z -score ≥ 15 as a
1014 difference between WT and *TBX5*^{in/del} paths.

1015 To identify differential expressed genes in inferred cardiac precursors (intermediate
1016 branches in the URD tree) that are affected by *TBX5* loss, cell barcodes from each precursor
1017 segment (wildtype/control/*TBX5*^{in/+} path vs. *TBX5*^{in/del} path) were extracted from the URD object
1018 and assigned new identities in the corresponding Seurat object. Differential gene test was then
1019 performed between the two segments using Wilcoxon Rank Sum test with `min.pct` set to 0.1 and

1020 logfc.threshold set to 0.25. Selected genes with an adjusted p-value less than 0.05 were plotted
1021 on the URD tree to visualize their expression.

1022 To compare the trident ($TNNT2^+$ distal branch for WTC11, control and $TBX5^{in/+}$) and fork
1023 ($TNNT2^+$ distal branch for $TBX5^{in/del}$) during pseudotime, we subdivided the pseudotime from the
1024 common branchpoint to the tips of the trident and fork into twenty uniform windows. Within each
1025 window, we then calculated the t test, difference of means, and fold change between the trident
1026 and fork for all genes. We filtered the statistics by gene-window combinations with adjusted p-
1027 value < 0.05 after Bonferroni-Holm multiple testing correction. Then, we hierarchically clustered
1028 the genes on t test p-values and plotted statistics using the R pheatmap library.

1029

1030 **Cell browser implementation.** The cell browser at cells.ucsc.edu was developed by Maximilian
1031 Haeussler. We created a cell browser session that allows the user to interrogate the spatial
1032 distribution of metadata and expression across data, in multiple reduced dimensionality spaces
1033 including the URD trajectory. Using a Scanpy python pipeline, we generated PCA, tSNE,
1034 UMAP, PAGA, and drl transforms. We also imported the URD trajectory mapping and WGCNA
1035 transform from their respective packages. We ran the scoreCT algorithm to assign cell types to
1036 cell clusters using a marker gene set.

1037

1038 **Gene regulatory network analysis.** bigScale2 (<https://github.com/iaconogi/bigScale2>) (Iacono
1039 et al., 2019; 2018) was used with default parameters to infer gene regulatory networks and
1040 “correlomes” from single cell RNA-seq expression data for $TNNT2^+$ cells. Expression counts and
1041 gene names were used as input from two technical replicates at each time point and $TBX5$
1042 genotype. Details of each dataset can be found in Table S6. To evaluate significant changes in
1043 pagerank or degree centrality, we computed all pairwise differential differences in pagerank or
1044 degree between baseline (wildtype and control) vs. $TBX5$ mutants ($TBX5^{in/+}$ or $TBX5^{in/del}$) (12
1045 total differences, from 2 $TBX5$ mutants * 2 baselines * 3 stages) and used these values to

1046 determine the top 5% upper change cutoff from 8,704 genes of all networks. Classification of
1047 Pearson correlations were empirically chosen at >0.5 for correlation and <-0.05 for anti-
1048 correlation.

1049

1050 **ChIP-seq.** Combined peaks of human TBX5 or GATA4 ChIP-seq from hiPSC-derived
1051 cardiomyocytes were used (Ang et al., 2016). bioChIP-seq of mouse TBX5, MEF2c and MEF2a
1052 from E12.5 hearts were from (Akerberg et al., 2019). Single replicates of TF bioChIP peaks,
1053 which were IDR normalized (IDR_THRESHOLD=0.05 between each set of replicates), were
1054 defined as the summit of the peak with the strongest ChIP signal \pm 100bp of the individual
1055 replicate with the greatest peak intensity. Mouse H3K27ac ChIP-seq at E12.5 of embryonic
1056 cardiac ventricles was from (He et al., 2014).

1057

1058 **QUANTIFICATION AND STATISTICAL ANALYSIS**

1059 **Scoring of sarcomeric disarray.** Myofibrillar arrangement in cardiomyocytes was manually
1060 scored on a scale of 1-5, similar to (Judge et al., 2017). A score of 1 represents cells with intact
1061 myofibrils in a parallel arrangement. A score of 2 represents cells that have intact myofibrils, but
1062 many are not parallel. Scores of 3 and 4 include cells with increasing degrees of myofibrillar
1063 fragmentation or aggregation. A score of 5 represents cells without visible myofibrils. No cells
1064 were apparent among our samples with a score of 5. Violin plots were generated in Prism
1065 (GraphPad) to show distribution of scored cells from each group. Fisher's exact test was used to
1066 determine statistical significance.

1067

1068 **Graphing and statistics for electrophysiology.** For electrophysiology and calcium imaging
1069 experiments, graphs were generated using Prism 8.2.0 (GraphPad Software). Significance
1070 between parental and experimental groups was determined with a custom R-script using

1071 unpaired two-sided Welch's *t* tests with Holm-Sidak correction for multiple comparisons
1072 (Holm1979). Adjusted p-value<0.05 was considered statistically significant.

1073

1074 **Statistical analyses for correlations.** We evaluated the pairwise association among 38
1075 variables, including all human genes, TBX5-dysregulated genes in human cardiomyocytes from
1076 day 23, CHD genes, EP genes, TBX5 or GATA4 binding (Ang et al., 2016), and genome-wide
1077 association (GWAS) genes for CHDs or arrhythmias (Cordell et al., 2013a; 2013b; Ellinor et al.,
1078 2012; Hoed et al., 2013; Hu et al., 2013; Pfeufer et al., 2010a; Smith et al., 2011). Reported
1079 GWAS genes from <https://www.ebi.ac.uk/gwas/> for the terms congenital heart disease,
1080 congenital heart malformation, congenital left sided heart lesions, conotruncal heart defect and
1081 aortic coarctation were used to define congenital heart disease-related (CHD) GWAS genes.
1082 Reported genes from terms such as cardiac arrhythmia, supraventricular ectopy, ventricular
1083 ectopy, premature cardiac contractions, atrial fibrillation, sudden cardiac arrest and ventricular
1084 fibrillation were considered as arrhythmia-related (EP-GWAS) genes. Two nearest genes within
1085 100kb, by using GREAT (great.stanford.edu) (McLean et al., 2010), of TBX5 or GATA4 binding
1086 sites or of reported genes from each group of GWAS, were considered for the analysis. The
1087 natural logarithm odds of genes associating with each one of these variables versus the odds of
1088 genes associating with every other variable were estimated using generalized linear models
1089 with family="binomial" setting in R. The resulting significance of these natural log odds ratios
1090 were adjusted for multiple testing by the Benjamini-Hochberg method (Benjamini and Hochberg,
1091 1995). Significance was determined using an FDR threshold of 0.05 or less.

1092 Additional correlations were evaluated between 26 variables, including human genes,
1093 human TBX5-dysregulated genes from day 23 cardiomyocytes, and TBX5, MEF2c or MEF2a
1094 binding sites from E12.5 mouse heart tissue (Akerberg et al., 2019). Human gene symbols were
1095 converted to mouse gene symbols, using the `getLDS()` function from the `biomaRt` package
1096 (<https://www.r-bloggers.com/convert-mouse-to-human-gene-names-with-biomart-package/>).

1097 Two nearest genes within 100kb of TBX5, MEF2c or MEF2a binding sites were considered for
1098 the analysis.

1099 For assessment of associations between binding locations of TBX5, MEF2c and MEF2a
1100 transcription factors with genes dysregulated by TBX5, analyses were performed corresponding
1101 to binding regions of each of the three TFs. First, binding regions of each TF was evaluated for
1102 association with genes, defined by the nearest two genes within 100kb. Using the list of human
1103 TBX5-dysregulated genes, binding regions of each TF associated with a TBX5-dysregulated
1104 gene was determined. Identified binding regions of each TF that overlapped with at least 50% of
1105 the binding regions of each of the other two TFs was determined, using bedops --element-of -
1106 50%. This approach defined three variables, including every binding region of the TF, if
1107 associated with a TBX5-dysregulated gene, or if it overlaps by at least 50% with the binding
1108 region of the other TFs, that were used for logistic regression in R. The resulting changes in
1109 odds are represented as natural logarithm odds ratios. Multiple testing correction was performed
1110 using the multtest package in R. All estimates are based on analyses for human TBX5-
1111 dysregulated genes.

1112

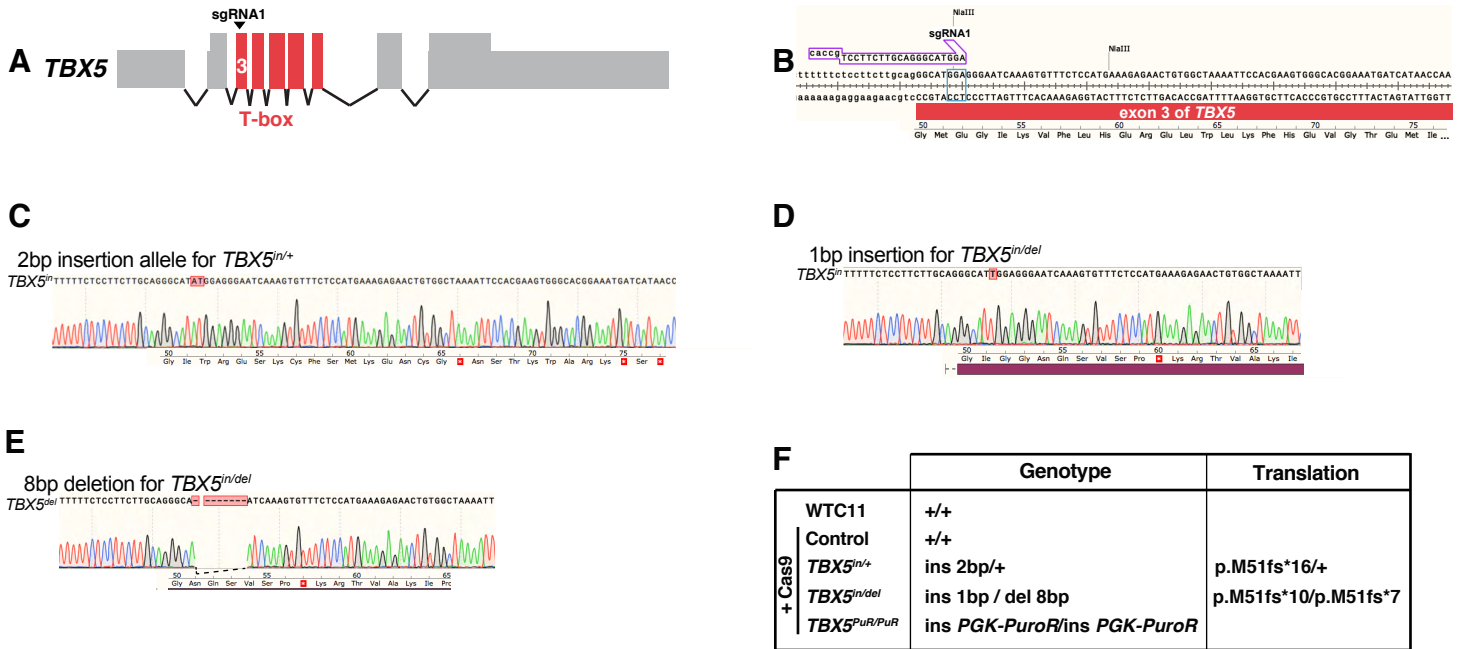
1113 **DATA AND SOFTWARE AVAILABILITY.** scRNA-seq datasets have been deposited at NCBI
1114 GEO, under accession GSE137876. R and python scripts will be available upon publication.

1115

1116

1117

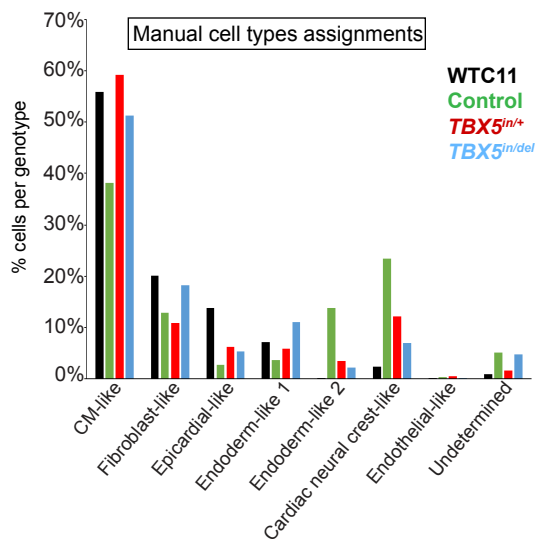
Figure S1



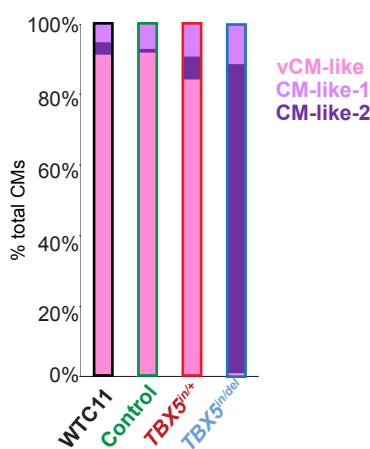
1118 **Figure S1. Genome editing of *TBX5* in human induced pluripotent stem cells.** (A) Diagram
1119 of the human *TBX5* gene. Exons encoding the T-box domain of *TBX5* are indicated in red.
1120 sgRNA1 was used to target exon 3 of *TBX5* by a CRISPR/Cas9 nuclease. (B) Sequence of the
1121 exon 3 of *TBX5* is shown, along with the sgRNA1 location. The PAM site is boxed in blue. Loss
1122 of the NlaIII site at the PAM site was used in initial screening for mutant iPS cell clones by PCR.
1123 The encoded wildtype protein sequence includes the start of the T-box domain. (C) Sequence
1124 and chromatogram for the 2bp insertion of the mutant allele for *TBX5*^{ins/+} predicts a premature
1125 truncation, as indicated by a stop codon (white asterisk in red box) in the frame-shifted protein
1126 sequence. (D, E) Sequence and chromatogram for the 1 bp insertion, or 8 bp deletion,
1127 respectively, of the mutant allele for *TBX5*^{ins/del}, along with corresponding protein sequences, are
1128 shown. (F) Table shows genotypes of WTC11-derived iPS cell lines that were targeted for *TBX5*
1129 at exon 3. Predicted translation for each *TBX5* genotype is indicated.
1130
1131

Figure S2

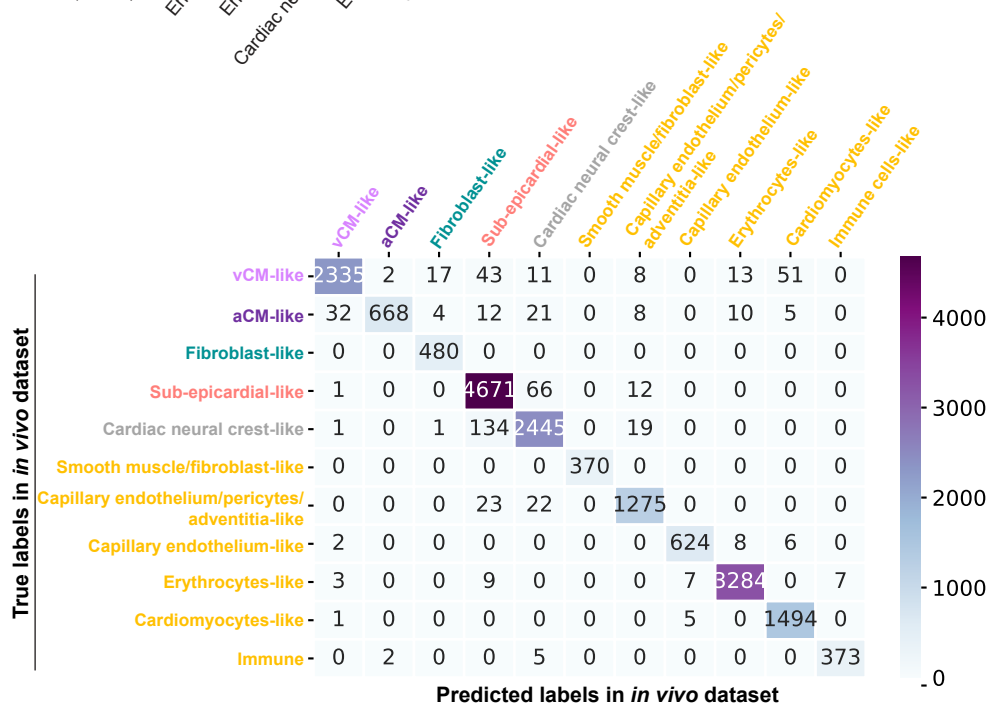
A



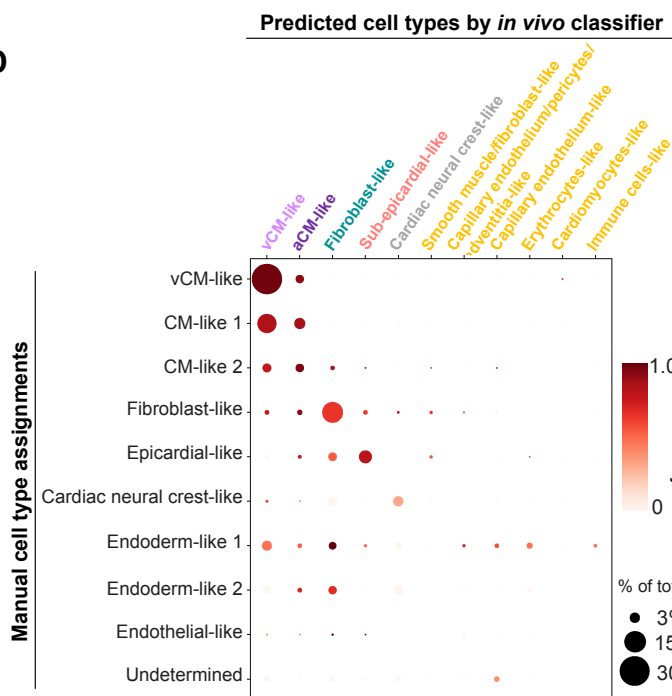
B



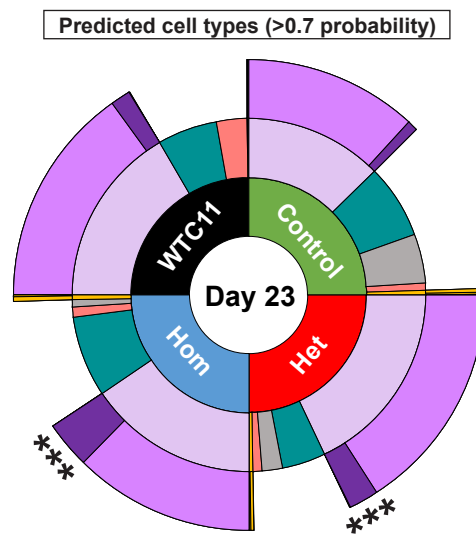
C



D

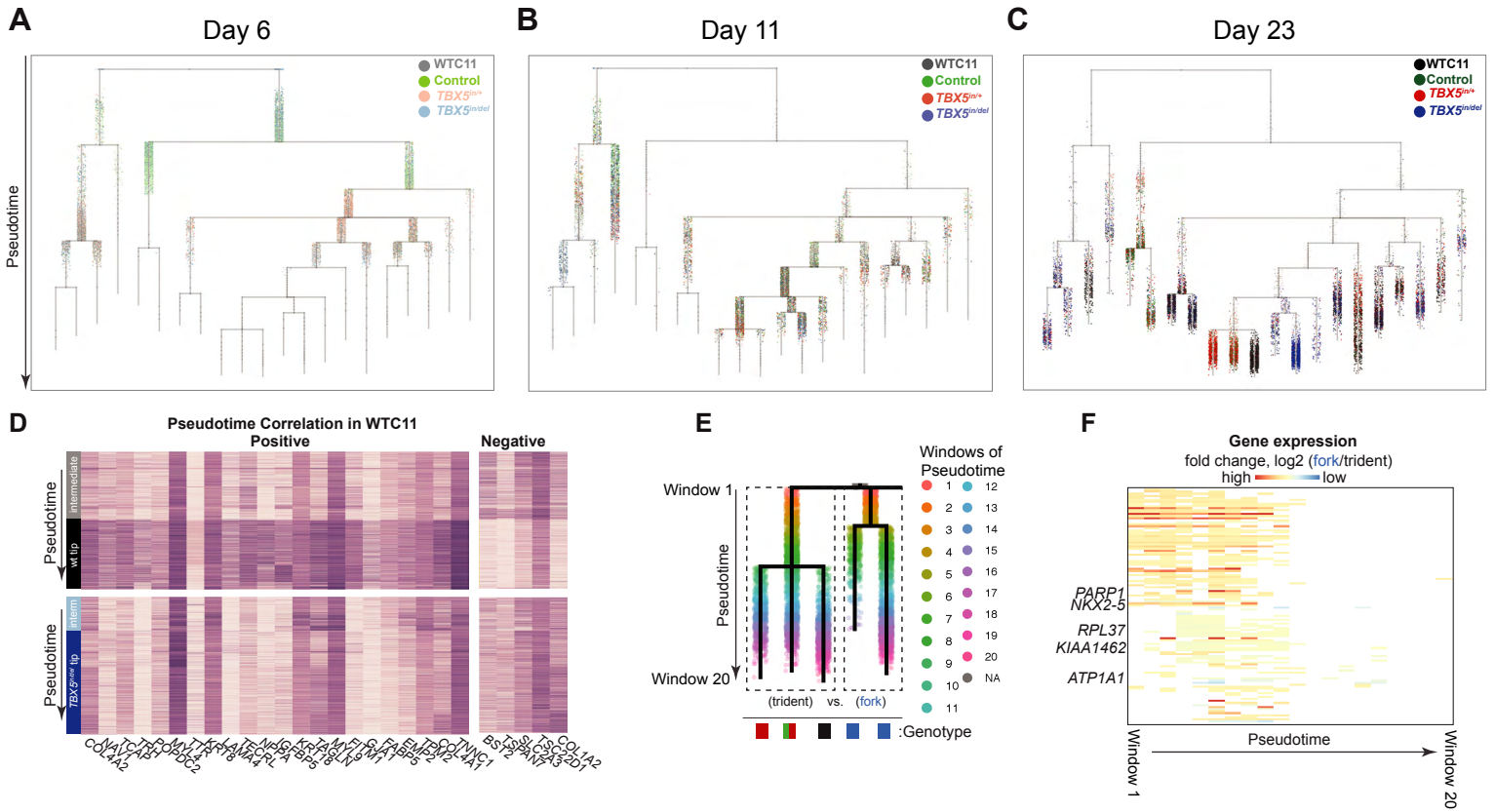


E



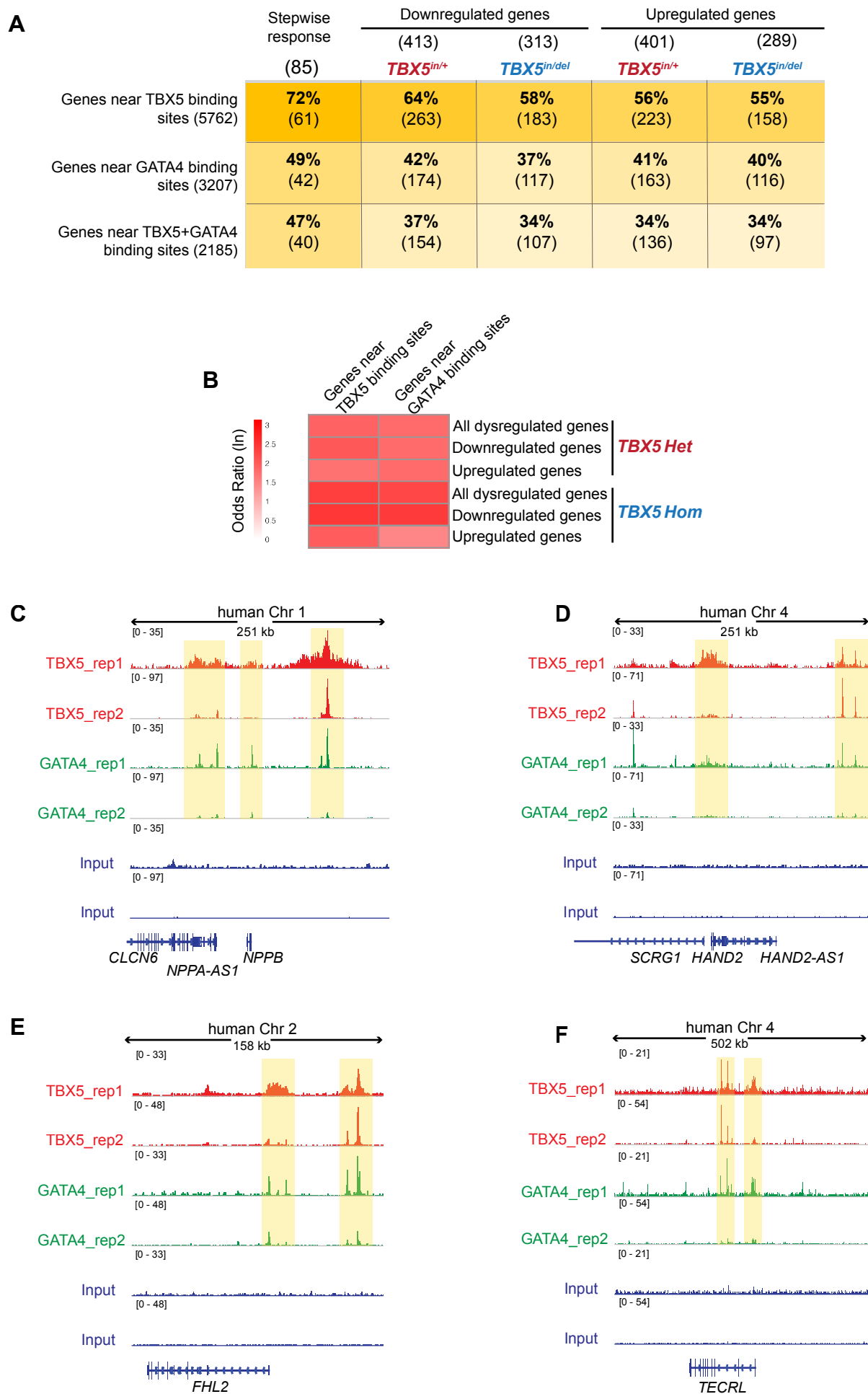
1132 **Figure S2. Diversity of iPSC-derived cell types by *TBX5* genotype.** (A) Manual assignment
1133 of iPSC-derived cell types by *TBX5* genotypes at day 23. (B) Distribution of iPSC-derived
1134 cardiomyocyte classification by *TBX5* genotype at day 23. (C) A confusion matrix compares test
1135 vs. predicted cell type labels for human fetal cardiac cells (Asp et al., 2019). (D) A confusion
1136 matrix compares cell type assignments of iPSC-derived cells at day 23 by manual annotation
1137 and *in vivo* classifier prediction. Color of each dot represents a prediction probability of the *in*
1138 *vivo* cell type classifier, while the dot size displays the percentage of the total iPSC-derived cells
1139 at day 23. (E) Distribution for predicted cell types of >0.7 prediction probability is shown by
1140 *TBX5* genotype at day 23 in a sunburst plot. *** $p < 0.0001$ by Fisher's exact test.
1141
1142

Figure S3

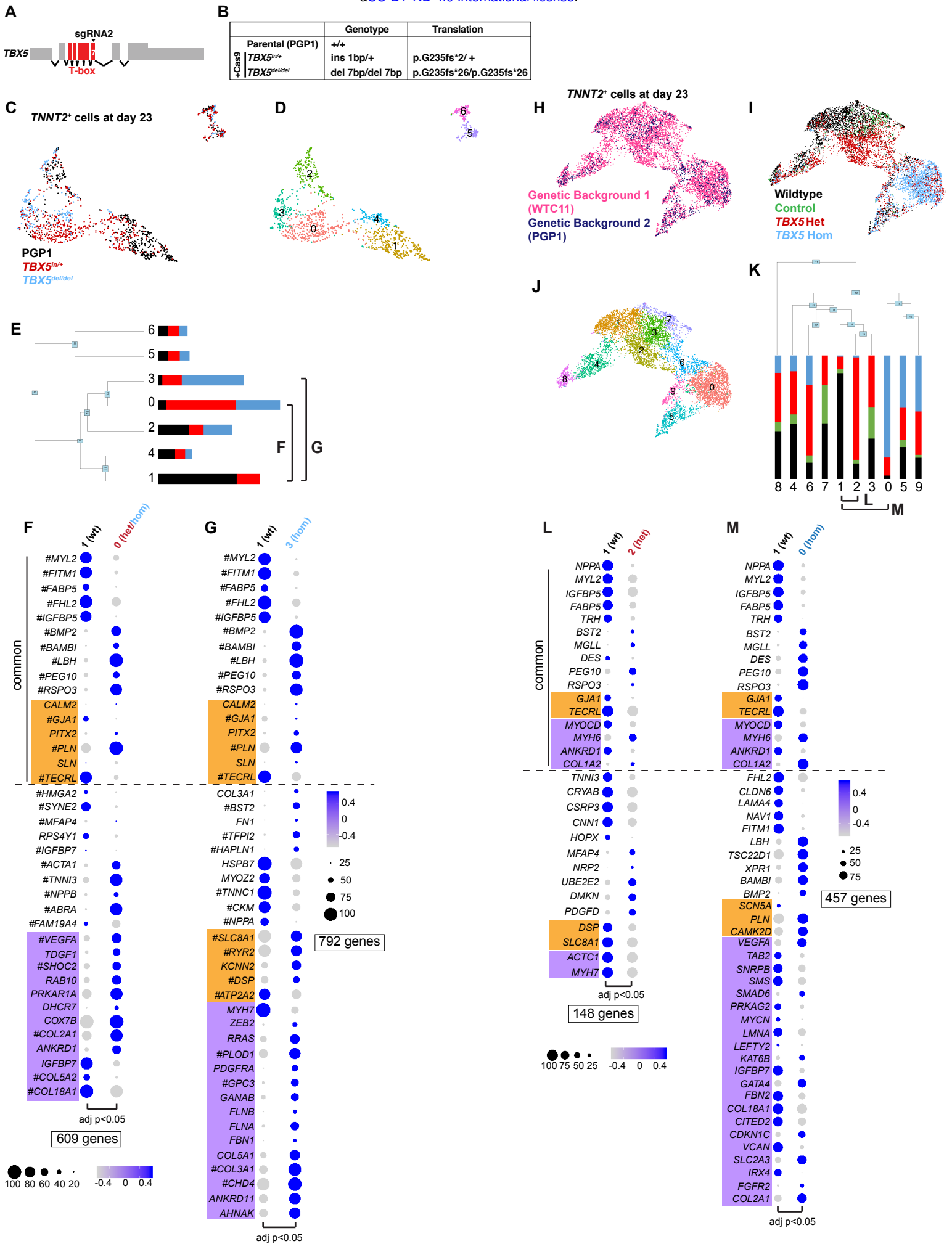


1143 **Figure S3. Pseudotime analysis of TBX5-dependent cardiomyocyte differentiation.** (A-C)
1144 Cells from all *TBX5* genotypes at day 6, 11 or 23 are shown by harvested time point on an
1145 aggregate pseudotime dendrogram using URD trajectory inferences. (D) Heatmaps show
1146 expression for each gene that displays a positive or negative correlation with pseudotime
1147 ($|\rho| \geq 0.4$ and Z-score ≥ 15 by difference in ρ) in the WT path (above) and is altered in the
1148 *TBX5^{in/del}* path (below). (E) Paths for WT/*TBX5^{in/+}* (trident) or *TBX5^{in/del}* (fork) to cardiomyocytes
1149 were divided into windows (1-20) along pseudotime for comparison. (F) Heatmap shows fold
1150 change for genes in a cluster that includes *NKX2-5*, which was significantly different after
1151 correction (adj p-value < 0.05 by Bonferroni-Holm test) in windows 2 through 8 between the
1152 deduced WT/control/ *TBX5^{in/+}* and *TBX5^{in/del}* paths, along with genes of a similar pattern,
1153 including *PARP1*, *RPL37*, *KIAA1462*, and *ATP1A1* (adj p-value < 0.05 by Bonferroni-Holm test).
1154
1155

Figure S4

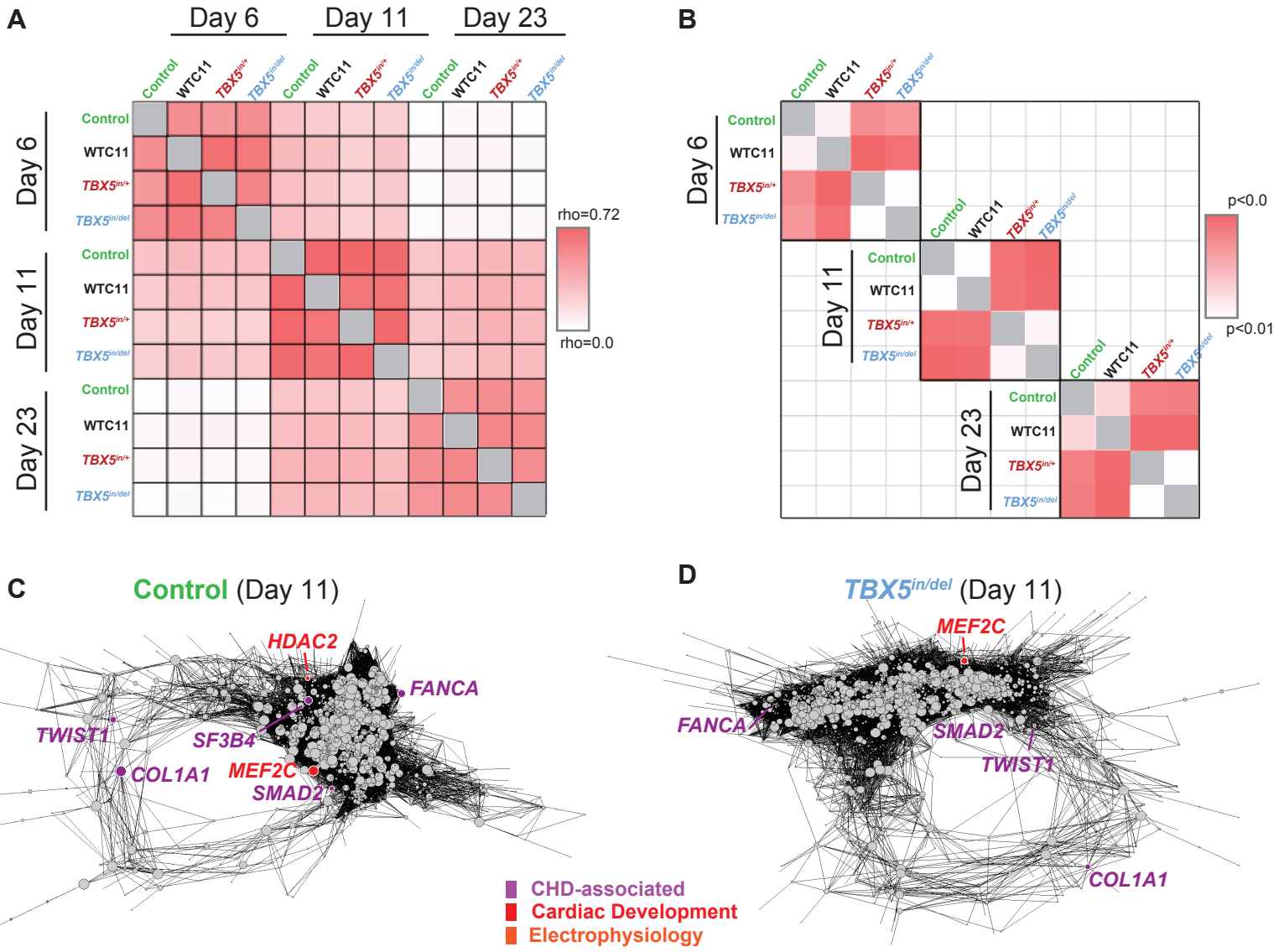


1156 **Figure S4. TBX5 and GATA4 occupancy near human TBX5-dependent genes.** (A) Table
1157 shows number of TBX5-dependent genes near TBX5, GATA4 or TBX5 and GATA4 occupancy
1158 (Ang et al., 2016). (B) Heatmap displays significant correlations (FDR<0.05) of TBX5 or GATA4
1159 occupancy near human TBX5-dependent gene sets (Table S5). Odds ratios for co-occupancy of
1160 TBX5 and GATA4 at TBX5-dependent genes are in Table S6. (B-E) Browser tracks of TBX5
1161 and GATA4 occupancy from iPSC-derived cardiomyocytes are shown for loci of TBX5-
1162 dependent genes *NPPA/NPPB*, *HAND2*, *FHL2* and *TECRL*.
1163
1164



1165 **Figure S5. Assessment of two genetic backgrounds for TBX5 dose-sensitive gene**
1166 **expression.** (A) Diagram of the human *TBX5* gene is shown, with exons in red. The guide
1167 sgRNA2 was used to target exon 7, which encodes a portion of the T-box domain, of *TBX5* in
1168 PGP1 iPS cells. (B) A table specifies each *TBX5* mutation and the predicted translation of *TBX5*
1169 for PGP1-derived *TBX5*^{in/+} or *TBX5*^{del/del} cells. (C, D) UMAPs of *TNNT2*⁺ cells at day 23 by *TBX5*
1170 genotype (C) or cluster identity (D). (E) A phylogenetic tree shows the relatedness of the
1171 'average' cell in each cluster using PC space. The percentage of cells within a cluster from
1172 each *TBX5* genotype are colored. Related clusters between different *TBX5* genotypes were
1173 compared for differential gene expression. (F, G) Dot plots show top differentially expressed
1174 genes in (F) *TBX5*^{in/+}- or (G) *TBX5*^{del/del}-enriched clusters. Significance was determined by
1175 Wilcoxon Rank Sum test (adj p-value<0.05) (Table S2). (H-J) *TNNT2*⁺ cells are displayed in a
1176 UMAP, by genetic background (WTC11 or PGP1-derived cells) (H), by *TBX5* genotype (I), or by
1177 Louvain clustering (J). (K) A phylogenetic tree shows the relatedness of the 'average' cell in
1178 each cluster using PC space. The proportion of cells in each cluster are colored by *TBX5*
1179 genotype. Related clusters between different *TBX5* genotypes were selected for differential
1180 gene tests. (L, M) Dot plots show top differentially expressed genes in (L) *TBX5*^{in/+}- or (M)
1181 *TBX5*^{del/del}-enriched clusters. Top five upregulated or downregulated differentially expressed
1182 genes, along with EP and CHD genes, were common between comparisons. Significance was
1183 determined by Wilcoxon Rank Sum test (adj p-value<0.05) (Table S2, S3).
1184
1185

Figure S6



1186 **Figure S6. Analysis of TBX5 dosage-sensitive gene regulatory networks.** (A) Correlation
1187 plot (Pearson correlations of pagerank centralities) of *TNNT2*⁺ networks by *TBX5* genotypes
1188 and time points are shown. Note that networks display highest similarity (red) within a time
1189 point. An inter-stage dissimilarity (white) grows proportionally to the time difference (i.e. day 23
1190 is less similar to day 6 than to day 11). Therefore, comparisons for genotype differences were
1191 made within differentiation stages. (C) Network similarity among *TBX5* genotypes within each
1192 time point is shown (Wilcoxon Rank Sum test of pagerank centralities for nodes from selected
1193 time point comparisons). (C, D) Network diagrams of *TNNT2*⁺ cells at day 11 for control (C) or
1194 *TBX5*^{in/del} (D) are shown.
1195
1196

1197 **Supplementary Tables.**

1198

1199 **Table S1.** Classifier gene features and weights for each cell type prediction.

1200

1201 **Table S2.** Lists of differential genes from comparisons between *TNNT2*⁺ clusters, at day 23 by
1202 biological replicate (Figure 4) or genetic background at day 23 (Figure S5).

1203

1204 **Table S3.** Curated gene lists, which are used in this study, include electrophysiology (EP)
1205 genes, human congenital heart disease (CHD) genes, mouse CHD genes, cardiac development
1206 genes, CHD-associated GWAS genes and EP-related GWAS genes.

1207

1208 **Table S4.** Correlation of human TBX5-dependent genes near TBX5 or GATA4 occupancy,
1209 congenital heart disease (CHD)-associated GWAS, electrophysiology (EP)-related GWAS, CHD
1210 genes, or EP genes. Odds ratios are displayed as natural logarithms. Statistical significance
1211 was determined by Benjamini-Hochberg multiple testing.

1212

1213 **Table S5.** Odds ratio as natural logarithm for transcription factor (TF) binding of TBX5 or
1214 GATA4 within 1kb of the other TF, near human TBX5-dependent genes. Statistical significance
1215 was determined by Benjamini-Hochberg multiple testing.

1216

1217 **Table S6.** TBX5-sensitive gene regulatory network analyses, by pagerank or degree, or by
1218 correlation with *TBX5* or *MEF2C* expression.

1219

1220 **Table S7.** Correlation of mouse orthologs of human TBX5-dependent genes near TBX5, MEF2c
1221 or MEF2a occupancy, congenital heart disease (CHD)-associated GWAS, electrophysiology
1222 (EP)-related GWAS, CHD genes, or EP genes. Odds ratios as natural logarithms are displayed.
1223 Statistical significance was determined by Benjamini-Hochberg multiple testing.

1224

1225 **Table S8.** Odds ratio as natural logarithms for transcription factor (TF) binding of TBX5, MEF2c,
1226 or MEF2a within 1kb of the other TFs in the trio, near mouse orthologs of human TBX5-
1227 dependent genes. Statistical significance was determined by Benjamini-Hochberg multiple
1228 testing.

1229

1230

1231

1232 REFERENCES.

- 1233 Abràmoff, M.D., Magalhães, P.J., and Ram, S.J. (2004). Image processing with ImageJ.
1234 *Biophotonics International* 11, 36–42.
- 1235 Akerberg, B.N., Gu, F., VanDusen, N.J., Zhang, X., Dong, R., Li, K., Zhang, B., Zhou, B., Sethi,
1236 I., Ma, Q., et al. (2019). A reference map of murine cardiac transcription factor chromatin
1237 occupancy identifies dynamic and conserved enhancers. *Nat Commun* 10, 4907.
- 1238 Ang, Y.-S., Rivas, R.N., Ribeiro, A.J.S., Srivas, R., Rivera, J., Stone, N.R., Pratt, K., Mohamed,
1239 T.M.A., Fu, J.-D., Spencer, C.I., et al. (2016). Disease Model of GATA4 Mutation Reveals
1240 Transcription Factor Cooperativity in Human Cardiogenesis. *Cell* 167, 1734–1749.e22.
- 1241 Asp, M., Giacomello, S., Larsson, L., Wu, C., Fürth, D., Qian, X., Wärdell, E., Custodio, J.,
1242 Reimegård, J., Salmén, F., et al. (2019). A Spatiotemporal Organ-Wide Gene Expression and
1243 Cell Atlas of the Developing Human Heart. *Cell* 179, 1647–1660.e19.
- 1244 Basson, C.T., Bachinsky, D.R., Lin, R.C., Levi, T., Elkins, J.A., Soultz, J., Grayzel, D.,
1245 Kroumpouzou, E., Traill, T.A., Leblanc-Straceski, J., et al. (1997). Mutations in human TBX5
1246 [corrected] cause limb and cardiac malformation in Holt-Oram syndrome. *Nat Genet* 15, 30–35.
- 1247 Basson, C.T., Cowley, G.S., Solomon, S.D., Weissman, B., Poznanski, A.K., Traill, T.A.,
1248 Seidman, J.G., and Seidman, C.E. (1994). The clinical and genetic spectrum of the Holt-Oram
1249 syndrome (heart-hand syndrome). *N Engl J Med* 330, 885–891.
- 1250 Becht, E., McInnes, L., Healy, J., Dutertre, C.-A., Kwok, I.W.H., Ng, L.G., Ginhoux, F., and
1251 Newell, E.W. (2018). Dimensionality reduction for visualizing single-cell data using UMAP. *Nat*
1252 *Biotechnol* 37, 38–44.
- 1253 Benjamini, Y., and Hochberg, Y. (1995). Controlling the False Discovery Rate - a Practical and
1254 Powerful Approach to Multiple Testing. *Journal of the Royal Statistical Society Series B-*
1255 *Statistical Methodology* 57, 289–300.
- 1256 Brin, S., and Page, L. (1998). The anatomy of a large-scale hypertextual Web search engine.
1257 *Computer Networks and Isdn Systems* 30, 107–117.
- 1258 Bruneau, B.G., Nemer, G., Schmitt, J.P., Charron, F., Robitaille, L., Caron, S., Conner, D.A.,
1259 Gessler, M., Nemer, M., Seidman, C.E., et al. (2001). A murine model of Holt-Oram syndrome
1260 defines roles of the T-box transcription factor Tbx5 in cardiogenesis and disease. *Cell* 106, 709–
1261 721.
- 1262 Butler, A., Hoffman, P., Smibert, P., Papalexi, E., and Satija, R. (2018). Integrating single-cell
1263 transcriptomic data across different conditions, technologies, and species. *Nat Biotechnol* 48,
1264 1070–17.
- 1265 Byrne, S.M., and Church, G.M. (2015). Crispr-mediated Gene Targeting of Human Induced
1266 Pluripotent Stem Cells. *Current Protocols in Stem Cell Biology* 35, 5A.8.1–A.8.22.
- 1267 Churko, J.M., Garg, P., Treutlein, B., Venkatasubramanian, M., Wu, H., Lee, J., Wessells, Q.N.,
1268 Chen, S.-Y., Chen, W.-Y., Chetal, K., et al. (2018). Defining human cardiac transcription factor
1269 hierarchies using integrated single-cell heterogeneity analysis. *Nat Commun* 9, 326–14.

- 1270 Cong, L., Ran, F.A., Cox, D., Lin, S., Barretto, R., Habib, N., Hsu, P.D., Wu, X., Jiang, W.,
1271 Marraffini, L.A., et al. (2013). Multiplex Genome Engineering Using CRISPR/Cas Systems.
1272 *Science* 339, 819–823.
- 1273 Cordell, H.J., Topf, A., Mamasoula, C., Postma, A.V., Bentham, J., Zelenika, D., Heath, S.,
1274 Blue, G., Cosgrove, C., Granados Riveron, J., et al. (2013a). Genome-wide association study
1275 identifies loci on 12q24 and 13q32 associated with Tetralogy of Fallot. *Hum Mol Genet* 22,
1276 1473–1481.
- 1277 Cordell, H.J., Bentham, J., Töpf, A., Zelenika, D., Heath, S., Mamasoula, C., Cosgrove, C.,
1278 Blue, G., Granados-Riveron, J., Setchfield, K., et al. (2013b). Genome-wide association study of
1279 multiple congenital heart disease phenotypes identifies a susceptibility locus for atrial septal
1280 defect at chromosome 4p16. *Nat Genet* 45, 822–824.
- 1281 Creemers, E.E., Sutherland, L.B., McAnally, J., Richardson, J.A., and Olson, E.N. (2006).
1282 Myocardin is a direct transcriptional target of Mef2, Tead and Foxo proteins during
1283 cardiovascular development. *Development* 133, 4245–4256.
- 1284 Dai, W., Laforest, B., Tyan, L., Shen, K.M., Nadadur, R.D., Alvarado, F.J., Mazurek, S.R.,
1285 Lazarevic, S., Gadek, M., Wang, Y., et al. (2019). A calcium transport mechanism for atrial
1286 fibrillation in *Tbx5*-mutant mice. *eLife* 8, 40.
- 1287 DeLaughter, D.M., Bick, A.G., Wakimoto, H., McKean, D., Gorham, J.M., Kathiriya, I.S., Hinson,
1288 J.T., Homsy, J., Gray, J., Pu, W., et al. (2016). Single-Cell Resolution of Temporal Gene
1289 Expression during Heart Development. *Dev Cell* 1–25.
- 1290 Devalla, H.D., Gélinas, R., Aburawi, E.H., Beqqali, A., Goyette, P., Freund, C., Chaix, M.A.,
1291 Tadros, R., Jiang, H., Le Béche, A., et al. (2016). *TECRL*, a new life-threatening inherited
1292 arrhythmia gene associated with overlapping clinical features of both LQTS and CPVT. *EMBO*
1293 *Mol Med* 8, 1390–1408.
- 1294 Devine, W.P., Wythe, J.D., George, M., Koshiba-Takeuchi, K., and Bruneau, B.G. (2014a).
1295 Early patterning and specification of cardiac progenitors in gastrulating mesoderm. *eLife* 3.
- 1296 Devine, W.P., Wythe, J.D., George, M., Koshiba-Takeuchi, K., and Bruneau, B.G. (2014b).
1297 Early patterning and specification of cardiac progenitors in gastrulating mesoderm. *eLife* 3.
- 1298 Driegen, S., Ferreira, R., van Zon, A., Strouboulis, J., Jaegle, M., Grosveld, F., Philipsen, S.,
1299 and Meijer, D. (2005). A generic tool for biotinylation of tagged proteins in transgenic mice.
1300 *Transgenic Res* 14, 477–482.
- 1301 Duan, J., Li, B., Bhakta, M., Xie, S., Zhou, P., Munshi, N.V., and Hon, G.C. (2019). Rational
1302 Reprogramming of Cellular States by Combinatorial Perturbation. *CellReports* 27, 3486–
1303 3499.e3486.
- 1304 Eisner, D.A., Caldwell, J.L., Trafford, A.W., and Hutchings, D.C. (2020). The Control of Diastolic
1305 Calcium in the Heart: Basic Mechanisms and Functional Implications. *Circ Res* 126, 395–412.
- 1306 Ellinor, P.T., Lunetta, K.L., Albert, C.M., Glazer, N.L., Ritchie, M.D., Smith, A.V., Arking, D.E.,
1307 Müller-Nurasyid, M., Krijthe, B.P., Lubitz, S.A., et al. (2012). Meta-analysis identifies six new
1308 susceptibility loci for atrial fibrillation. *Nat Genet* 44, 670–675.

- 1309 Farrell, J.A., Wang, Y., Riesenfeld, S.J., Shekhar, K., Regev, A., and Schier, A.F. (2018a).
1310 Single-cell reconstruction of developmental trajectories during zebrafish embryogenesis.
1311 *Science* 360, eaar3131–eaar3139.
- 1312 Farrell, J.A., Wang, Y., Riesenfeld, S.J., Shekhar, K., Regev, A., and Schier, A.F. (2018b).
1313 Single-cell reconstruction of developmental trajectories during zebrafish embryogenesis.
1314 *Science* 108, eaar3131–eaar3139.
- 1315 Fisher, R.A. (1921). On the “Probable Error” of a Coefficient of Correlation Deduced from a
1316 Small Sample. *Metron* 1, 3–32.
- 1317 Garg, V., Kathiriya, I.S., Barnes, R., Schluterman, M.K., King, I.N., Butler, C.A., Rothrock, C.R.,
1318 Eapen, R.S., Hirayama-Yamada, K., Joo, K., et al. (2003). GATA4 mutations cause human
1319 congenital heart defects and reveal an interaction with TBX5. 424, 443–447.
- 1320 Ghosh, T.K., Song, F.F., Packham, E.A., Buxton, S., Robinson, T.E., Ronksley, J., Self, T.,
1321 Bonser, A.J., and Brook, J.D. (2009). Physical interaction between TBX5 and MEF2C is
1322 required for early heart development. *Mol Cell Biol* 29, 2205–2218.
- 1323 Gifford, C.A., Ranade, S.S., Samarakoon, R., Salunga, H.T., de Soysa, T.Y., Huang, Y., Zhou,
1324 P., Elfenbein, A., Wyman, S.K., Bui, Y.K., et al. (2019). Oligogenic inheritance of a human heart
1325 disease involving a genetic modifier. *Science* 364, 865–870.
- 1326 Hafemeister, C., and Satija, R. (2019). Normalization and variance stabilization of single-cell
1327 RNA-seq data using regularized negative binomial regression. *Genome Biol* 20, 296–15.
- 1328 He, A., Gu, F., Hu, Y., Ma, Q., Yi Ye, L., Akiyama, J.A., Visel, A., Pennacchio, L.A., and Pu,
1329 W.T. (2014). Dynamic GATA4 enhancers shape the chromatin landscape central to heart
1330 development and disease. *Nat Commun* 5, 4907.
- 1331 Hiroi, Y., Kudoh, S., Monzen, K., Ikeda, Y., Yazaki, Y., Nagai, R., and Komuro, I. (2001). Tbx5
1332 associates with Nkx2-5 and synergistically promotes cardiomyocyte differentiation. *Nat Genet*
1333 28, 276–280.
- 1334 Hoed, den, M., Eijgelsheim, M., Esko, T., Brundel, B.J.J.M., Peal, D.S., Evans, D.M., Nolte, I.M.,
1335 Segrè, A.V., Holm, H., Handsaker, R.E., et al. (2013). Identification of heart rate–associated loci
1336 and their effects on cardiac conduction and rhythm disorders. *Nat Genet* 45, 621–631.
- 1337 Hoffman, J.I. (1995). Incidence of congenital heart disease: II. Prenatal incidence. *Pediatr*
1338 *Cardiol* 16, 155–165.
- 1339 Hoffman, J.I.E., and Kaplan, S. (2002). The incidence of congenital heart disease. *J Am Coll*
1340 *Cardiol* 39, 1890–1900.
- 1341 Holm, S., 1979 A simple sequentially rejective multiple test procedure. *Scandinavian Journal of*
1342 *Statistics* 6, 65–70.
- 1343 Homsy, J., Zaidi, S., Shen, Y., Ware, J.S., Samocha, K.E., Karczewski, K.J., DePalma, S.R.,
1344 McKean, D., Wakimoto, H., Gorham, J., et al. (2015). De novo mutations in congenital heart
1345 disease with neurodevelopmental and other congenital anomalies. *Science* 350, 1262–1266.

- 1346 Hookway, T.A., Matthys, O.B., Mendoza-Camacho, F.N., Rains, S., Sepulveda, J.E., Joy, D.A.,
1347 and McDevitt, T.C. (2019). Phenotypic Variation Between Stromal Cells Differentially Impacts
1348 Engineered Cardiac Tissue Function. *Tissue Engineering Part A* 25, 773–785.
- 1349 Hu, Z., Shi, Y., Mo, X., Xu, J., Zhao, B., Lin, Y., Yang, S., Xu, Z., Dai, J., Pan, S., et al. (2013). A
1350 genome-wide association study identifies two risk loci for congenital heart malformations in Han
1351 Chinese populations. *Nat Genet* 45, 818–821.
- 1352 Iacono, G., Massoni-Badosa, R., and Heyn, H. (2019). Single-cell transcriptomics unveils gene
1353 regulatory network plasticity. 1–20.
- 1354 Iacono, G., Mereu, E., Guillaumet-Adkins, A., Corominas, R., Cuscó, I., Rodríguez-Esteban, G.,
1355 Gut, M., Pérez-Jurado, L.A., Gut, I., and Heyn, H. (2018). bigScale: an analytical framework for
1356 big-scale single-cell data. *Genome Research* 28, 878–890.
- 1357 Jin, S.C., Homsy, J., Zaidi, S., Lu, Q., Morton, S., DePalma, S.R., Zeng, X., Qi, H., Chang, W.,
1358 Sierant, M.C., et al. (2017). Contribution of rare inherited and de novo variants in 2,871
1359 congenital heart disease probands. *Nat Genet* 49, 1593–1601.
- 1360 Judge, L.M., Perez-Bermejo, J.A., Truong, A., Ribeiro, A.J.S., Yoo, J.C., Jensen, C.L.,
1361 Mandegar, M.A., Huebsch, N., Kaake, R.M., So, P.-L., et al. (2017). A BAG3 chaperone
1362 complex maintains cardiomyocyte function during proteotoxic stress. *JCI Insight* 2, 83–18.
- 1363 Karakikes, I., Termglinchan, V., Cepeda, D.A., Lee, J., Diecke, S., Hendel, A., Itzhaki, I.,
1364 Ameen, M., Shrestha, R., Wu, H., et al. (2017). A Comprehensive TALEN-Based Knockout
1365 Library for Generating Human-Induced Pluripotent Stem Cell-Based Models for Cardiovascular
1366 Diseases. *Circ Res* 120, 1561–1571.
- 1367 Karczewski, K.J., Francioli, L.C., Tiao, G., Cummings, B.B., Alfoldi, J., Wang, Q., Collins, R.L.,
1368 Laricchia, K.M., Ganna, A., and Birnbaum, D.P., et al. (2020). Variation across 141,456 human
1369 exomes and genomes reveals the spectrum of loss-of-function intolerance across human
1370 protein-coding genes. *Biorxiv.org*.
- 1371 Laforest, B., Dai, W., Tyan, L., Lazarevic, S., Shen, K.M., Gadek, M., Broman, M.T., Weber,
1372 C.R., and Moskowitz, I.P. (2019). Atrial fibrillation risk loci interact to modulate Ca²⁺-dependent
1373 atrial rhythm homeostasis. *J Clin Invest* 412, 1825–15.
- 1374 Lalani, S.R., and Belmont, J.W. (2014). Genetic basis of congenital cardiovascular
1375 malformations. *Eur J Med Genet* 57, 402–413.
- 1376 Lee, J.-H., Park, I.-H., Gao, Y., Li, J.B., Li, Z., Daley, G.Q., Zhang, K., and Church, G.M. (2009).
1377 A Robust Approach to Identifying Tissue-Specific Gene Expression Regulatory Variants Using
1378 Personalized Human Induced Pluripotent Stem Cells. *PLoS Genet* 5, e1000718–15.
- 1379 Li, G., Xu, A., Sim, S., Priest, J.R., Tian, X., Khan, T., Quertermous, T., Zhou, B., Tsao, P.S.,
1380 Quake, S.R., et al. (2016). Transcriptomic Profiling Maps Anatomically Patterned
1381 Subpopulations among Single Embryonic Cardiac Cells. *Dev Cell* 39, 491–507.
- 1382 Li, Q.Y., Newbury-Ecob, R.A., Terrett, J.A., Wilson, D.I., Curtis, A.R., Yi, C.H., Gebuhr, T.,
1383 Bullen, P.J., Robson, S.C., Strachan, T., et al. (1997). Holt-Oram syndrome is caused by
1384 mutations in TBX5, a member of the Brachyury (T) gene family. *Nat Genet* 15, 21–29.

- 1385 Lin, Q., Schwarz, J., Bucana, C., and Olson, E.N. (1997). Control of mouse cardiac
1386 morphogenesis and myogenesis by transcription factor MEF2C. *Science* 276, 1404–1407.
- 1387 Luna-Zurita, L., Stirnimann, C.U., Glatt, S., Kaynak, B.L., Thomas, S., Baudin, F., Samee,
1388 M.A.H., He, D., Small, E.M., Mileikovsky, M., et al. (2016). Complex Interdependence Regulates
1389 Heterotypic Transcription Factor Distribution and Coordinates Cardiogenesis. *Cell* 164, 999–
1390 1014.
- 1391 Lyons, I., Parsons, L.M., Hartley, L., Li, R., Andrews, J.E., Robb, L., and Harvey, R.P. (1995).
1392 Myogenic and morphogenetic defects in the heart tubes of murine embryos lacking the homeo
1393 box gene *Nkx2-5*. *9*, 1654–1666.
- 1394 Maitra, M., Schluterman, M.K., Nichols, H.A., Richardson, J.A., Lo, C.W., Srivastava, D., and
1395 Garg, V. (2009). Interaction of *Gata4* and *Gata6* with *Tbx5* is critical for normal cardiac
1396 development. *326*, 368–377.
- 1397 Mandegar, M.A., Huebsch, N., Frolov, E.B., Shin, E., Truong, A., Olvera, M.P., Chan, A.H.,
1398 Miyaoka, Y., Holmes, K., Spencer, C.I., et al. (2016). CRISPR Interference Efficiently Induces
1399 Specific and Reversible Gene Silencing in Human iPSCs. *Cell Stem Cell* 18, 541–553.
- 1400 McCulley, D.J., and Black, B.L. (2012). Transcription factor pathways and congenital heart
1401 disease. *Curr. Top. Dev. Biol.* 100, 253–277.
- 1402 McDermott, D.A., Hatcher, C.J., and Basson, C.T. (2008). Atrial Fibrillation and Other Clinical
1403 Manifestations of Altered *TBX5* Dosage in Typical Holt-Oram Syndrome. *Circ Res* 103, e96.
- 1404 McLean, C.Y., Bristor, D., Hiller, M., Clarke, S.L., Schaar, B.T., Lowe, C.B., Wenger, A.M., and
1405 Bejerano, G. (2010). GREAT improves functional interpretation of cis-regulatory regions. *Nat*
1406 *Biotechnol* 28, 495–501.
- 1407 Miyaoka, Y., Chan, A.H., Judge, L.M., Yoo, J., Huang, M., Nguyen, T.D., Lizarraga, P.P., So, P.-
1408 L., and Conklin, B.R. (2014). Isolation of single-base genome-edited human iPSC cells without
1409 antibiotic selection. *Nat Meth* 11, 291–293.
- 1410 Mori, A.D., and Bruneau, B.G. (2004). *TBX5* mutations and congenital heart disease: Holt-Oram
1411 syndrome revealed. *Curr Opin Cardiol* 19, 211–215.
- 1412 Mori, A.D., Zhu, Y., Vahora, I., Nieman, B., Koshiba-Takeuchi, K., Davidson, L., Pizard, A.,
1413 Seidman, J.G., Seidman, C.E., Chen, X.J., et al. (2006). *Tbx5*-dependent rheostatic control of
1414 cardiac gene expression and morphogenesis. *297*, 566–586.
- 1415 Nadadur, R.D., Broman, M.T., Boukens, B., Mazurek, S.R., Yang, X., van den Boogaard, M.,
1416 Bekeny, J., Gadek, M., Ward, T., Zhang, M., et al. (2016). *Pitx2* modulates a *Tbx5*-dependent
1417 gene regulatory network to maintain atrial rhythm. *Science Translational Medicine* 8, 354ra115–
1418 354ra115.
- 1419 Nora, E.P., Goloborodko, A., Valton, A.-L., Gibcus, J.H., Uebersohn, A., Abdennur, N., Dekker,
1420 J., Mirny, L.A., and Bruneau, B.G. (2017). Targeted Degradation of CTCF Decouples Local
1421 Insulation of Chromosome Domains from Genomic Compartmentalization. *Cell* 169, 930–
1422 933.e22.

- 1423 Panesar, D.K., and Burch, M. (2017). Assessment of Diastolic Function in Congenital Heart
1424 Disease. *Front. Cardiovasc. Med.* 4, 2254–10.
- 1425 Pedregosa, F., Varoquaux, G., Gramfort, A., Michel, V., Thirion, B., Grisel, O., Blondel, M.,
1426 Prettenhofer, P., Weiss, R., Dubourg, V., et al. (2011). Scikit-learn: Machine Learning in Python.
1427 *Journal of Machine Learning Research* 12, 2825–2830.
- 1428 Peters, D.T., Cowan, C.A., and Musunuru, K. (2008). Genome editing in human pluripotent stem
1429 cells (Cambridge (MA): Harvard Stem Cell Institute).
- 1430 Pfeufer, A., van Noord, C., Marciante, K.D., Arking, D.E., Larson, M.G., Smith, A.V., Tarasov,
1431 K.V., Müller, M., Sotoodehnia, N., Sinner, M.F., et al. (2010a). Genome-wide association study
1432 of PR interval. *Nat Genet* 42, 153–159.
- 1433 Pfeufer, A., van Noord, C., Marciante, K.D., Arking, D.E., Larson, M.G., Smith, A.V., Tarasov,
1434 K.V., Müller, M., Sotoodehnia, N., Sinner, M.F., et al. (2010b). Genome-wide association study
1435 of PR interval. *Nat Genet* 42, 153–159.
- 1436 Phan, D., Rasmussen, T.L., Nakagawa, O., McAnally, J., Gottlieb, P.D., Tucker, P.W.,
1437 Richardson, J.A., Bassel-Duby, R., and Olson, E.N. (2005). BOP, a regulator of right ventricular
1438 heart development, is a direct transcriptional target of MEF2C in the developing heart.
1439 *Development* 132, 2669–2678.
- 1440 Prendiville, T., Jay, P.Y., and Pu, W.T. (2014). Insights into the genetic structure of congenital
1441 heart disease from human and murine studies on monogenic disorders. *Cold Spring Harb*
1442 *Perspect Med* 4, a013946–a013946.
- 1443 Priest, J.R., Osoegawa, K., Mohammed, N., Nanda, V., Kundu, R., Schultz, K., Lammer, E.J.,
1444 Girirajan, S., Scheetz, T., Waggott, D., et al. (2016). De Novo and Rare Variants at Multiple Loci
1445 Support the Oligogenic Origins of Atrioventricular Septal Heart Defects. *PLoS Genet* 12,
1446 e1005963–25.
- 1447 Satija, R., Farrell, J.A., Gennert, D., Schier, A.F., and Regev, A. (2015). Spatial reconstruction
1448 of single-cell gene expression data. *Nat Biotechnol* 33, 495–502.
- 1449 Sifrim, A., Hitz, M.-P., Wilsdon, A., Breckpot, J., Turki, A.I., S.H., Thienpont, B., McRae, J.,
1450 Fitzgerald, T.W., Singh, T., Swaminathan, G.J., et al. (2016). Distinct genetic architectures for
1451 syndromic and nonsyndromic congenital heart defects identified by exome sequencing. *Nat*
1452 *Genet* 48, 1060–1065.
- 1453 Smith, J.G., Magnani, J.W., Palmer, C., Meng, Y.A., Soliman, E.Z., Musani, S.K., Kerr, K.F.,
1454 Schnabel, R.B., Lubitz, S.A., Sotoodehnia, N., et al. (2011). Genome-Wide Association Studies
1455 of the PR Interval in African Americans. *PLoS Genet* 7, e1001304.
- 1456 Spencer, C.I., Baba, S., Nakamura, K., Hua, E.A., Sears, M.A.F., Fu, C.-C., Zhang, J.,
1457 Balijepalli, S., Tomoda, K., Hayashi, Y., et al. (2014). Calcium Transients Closely Reflect
1458 Prolonged Action Potentials in iPSC Models of Inherited Cardiac Arrhythmia. *Stem Cell Reports*
1459 1–13.
- 1460 Stathopoulos, A., and Levine, M. (2002). Dorsal Gradient Networks in the Drosophila Embryo.
1461 *246*, 57–67.

- 1462 Stuart, T., Butler, A., Hoffman, P., Hafemeister, C., Papalexi, E., Mauck, W.M., III, Hao, Y.,
1463 Stoeckius, M., Smibert, P., and Satija, R. (2019). Comprehensive Integration of Single-Cell
1464 Data. *Cell* 1–37.
- 1465 Tanaka, M., Chen, Z., Bartunkova, S., Yamasaki, N., and Izumo, S. (1999). The cardiac
1466 homeobox gene *Csx/Nkx2.5* lies genetically upstream of multiple genes essential for heart
1467 development. *Development* 126, 1269–1280.
- 1468 Theodoris, C.V., Li, M., White, M.P., Liu, L., He, D., Pollard, K.S., Bruneau, B.G., and
1469 Srivastava, D. (2015). Human disease modeling reveals integrated transcriptional and
1470 epigenetic mechanisms of NOTCH1 haploinsufficiency. *Cell* 160, 1072–1086.
- 1471 Waldron, L., Steimle, J.D., Greco, T.M., Gomez, N.C., Dorr, K.M., Kweon, J., Temple, B., Yang,
1472 X.H., Wilczewski, C.M., Davis, I.J., et al. (2016). The Cardiac TBX5 Interactome Reveals a
1473 Chromatin Remodeling Network Essential for Cardiac Septation. *Dev Cell* 36, 262–275.
- 1474 Zaidi, S., and Brueckner, M. (2017). Genetics and Genomics of Congenital Heart Disease. *Circ
1475 Res* 120, 923–940.
- 1476 Zaidi, S., Choi, M., Wakimoto, H., Ma, L., Jiang, J., Overton, J.D., Romano-Adesman, A.,
1477 Bjornson, R.D., Breitbart, R.E., Brown, K.K., et al. (2013). De novo mutations in histone-
1478 modifying genes in congenital heart disease. *498*, 220–223.
- 1479 Zhou, Y.-Q., Zhu, Y., Bishop, J., Davidson, L., Henkelman, R.M., Bruneau, B.G., and Foster,
1480 F.S. (2005). Abnormal cardiac inflow patterns during postnatal development in a mouse model
1481 of Holt-Oram syndrome. *Am J Physiol Heart Circ Physiol* 289, H992–H1001.
- 1482 Zhu, Y., Gramolini, A.O., Walsh, M.A., Zhou, Y.-Q., Slorach, C., Friedberg, M.K., Takeuchi, J.K.,
1483 Sun, H., Henkelman, R.M., Backx, P.H., et al. (2008). *Tbx5*-dependent pathway regulating
1484 diastolic function in congenital heart disease. *Proceedings of the National Academy of Sciences*
1485 105, 5519–5524.